Volume 54
Number 46
14 December 2025
Pages 16995-17348

Dalton Transactions

An international journal of inorganic chemistry

rsc.li/dalton

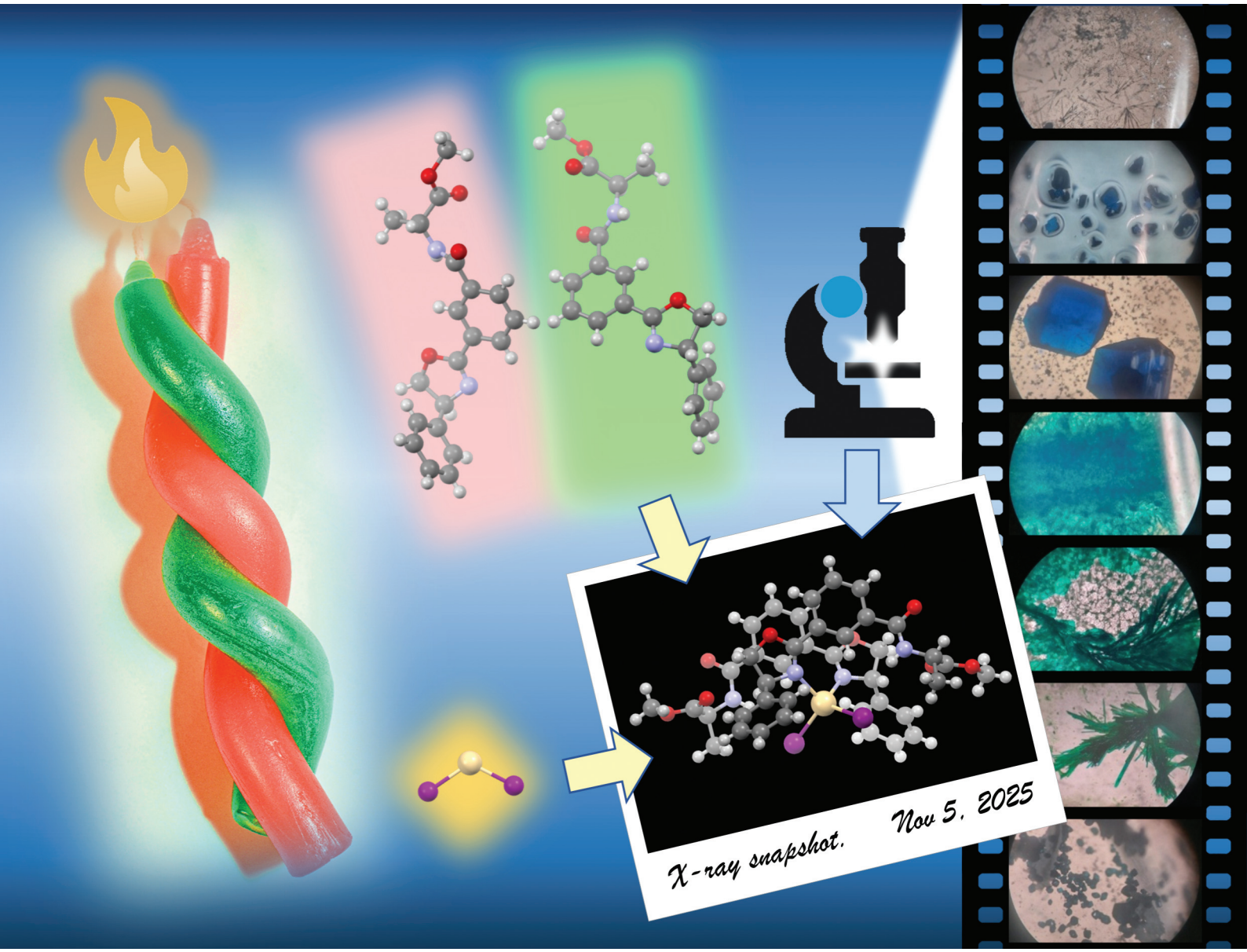

ISSN 1477-9226

ROYAL SOCIETY OF CHEMISTRY

PAPER

Srećko I. Kirin *et al.*

Induction of helical chirality in tetrahedral transition metal complexes with non-bridging monodentate oxazolines

Dalton Transactions

ROYAL SOCIETY OF CHEMISTRY

PAPER

View Article Online
View Journal | View Issue

Check for updates

Cite this: *Dalton Trans.*, 2025, **54**, 17083

Induction of helical chirality in tetrahedral transition metal complexes with non-bridging monodentate oxazolines

Marija Bakija, Berislav Perić, Tamara Rinkovec, Ernest Sanders, Zoran Kokan, Zoran Štefanić, Robert Vianello and Srećko I. Kirin *

Received 7th October 2025,
Accepted 5th November 2025

DOI: 10.1039/d5dt02399h

rsc.li/dalton

Chirality on C4-atoms of non-bridging monodentate oxazolines direct stereoselective formation of helical chirality in $[M(\mathbf{1})_2X_2]$ tetrahedral metal complexes of zinc(II), cadmium(II) and cobalt(II) halides, as revealed by their crystal structures. This feature was used to prepare a set of helically chiral derivatives with various structural motifs. In particular, bulkiness, non-covalent interactions and choice of point chirality combinations were found to strongly affect induction of chirality on the metal atom. The substituent influence on complexation and chiral induction was analyzed using XRD-diffraction studies, NMR, UV-Vis and CD spectroscopies, as well as DFT calculations.

Introduction

Chirality is a fundamental property of molecular structure that plays a vital part in chemical interactions. In particular, controlling chirality is crucial in the preparation of a great variety of compounds, ranging from chiral drugs in medicinal chemistry[1] and stereoselective catalysts in both academic and industrial laboratories,[2,3] to advanced functional materials[4,5] and sensors.[6] In majority of cases, the source of chirality in metal complexes can be grouped into two notable types, chiral-at-metal complexes[7–10] and metal complexes with chiral ligands[10–15] (Fig. 1a and b, respectively). The former type of metal complexes is obtained either by forming a chiral metal centre through coordination by four or more different ligands (Fig. 1a, left) or through coordination by achiral ligands with non-interchangeable, stereoisomeric spatial organization (Fig. 1a, right).[16] Although it was found that certain combinations of metals and ligands may prefer a specific spatial organization,[17,18] various strategies usually must be employed in order to avoid racemic contamination.

Metal complexes with chiral ligands usually contain rigid multidentate ligands with chirality typically incorporated close to the coordinating atoms (Fig. 1b, left). In addition, the chirality integrated into ligands of metal complexes is not limited just to chiral centres, rather, numerous applications of metal complexes with ligands containing axial[19] and helical chirality are known.[10] An interesting subtype of metal complexes with chiral ligands is based on metal complexes with "backdoor induction" of chirality (Fig. 1b, right). In these compounds, chirality is incorporated several bonds away from the coordinating ligand atoms and the chiral information is transmitted to the metal atom *via* a chiral structure that forms as a consequence of non-covalent inter-ligand interactions.[20] Specific motifs of hydrogen bonding that are known to induce chirality in this manner have been previously described on 1,*n*′-disubstituted ferrocene peptides (Fig. 2), namely, Herrick, van Staveren and Xu conformations with two, one or without hydrogen bonds, respectively.[21–23]

2-Oxazoline ligands are known for their application in catalysis and as precursors in polymer synthesis.[24,25] Their success as ligands for metal complexes partially lies in their facile synthesis from easily available carboxylic acids or nitriles and amino alcohols.[26] One of the most noteworthy chiral metal

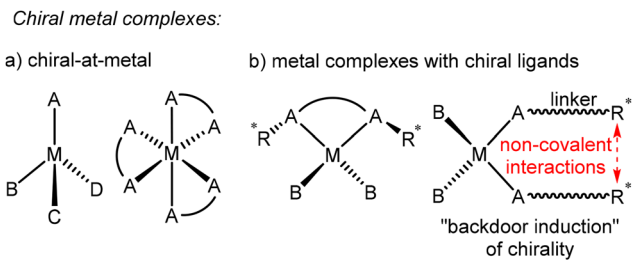

Fig. 1 (a) Chiral-at-metal complexes with four different ligands (a, left) or with a stereoisomeric spatial arrangement of achiral ligands (a, right). (b) Metal complexes with chiral ligands in which the chirality (group R*) is adjacent to the metal center (b, left) or placed several covalent bonds away and the chiral information is transmitted to the metal center as a consequence of non-covalent inter-ligand interactions (b, right).

Ruđer Bošković Institute, Bijenička c. 54, HR-10000 Zagreb, Croatia.
E-mail: Srecko.Kirin@irb.hr

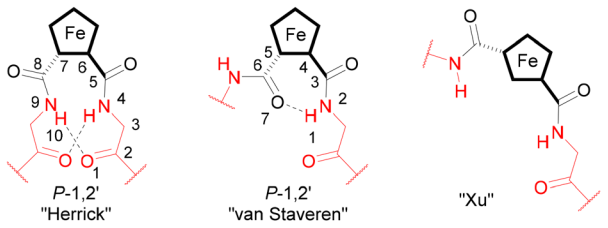

Fig. 2 Hydrogen bonding motifs in substituted 1,*n*′-ferrocenyl peptides. Bold lines represent bonds spatially in front of the rest of the molecule, and dashed lines represent bonds spatially behind the rest of the molecule.

complexes of oxazolines feature bisoxazoline ligands (BOX) with C4-chiral carbon atoms.[24,27] The structure of these ligands play a critical role in steric control, by providing an appropriate and rigid chelating structure and an environment necessary for chiral induction.[24] Further efforts to control the chirality of the coordination sphere mainly focused on utilizing the rigid nature of polymeric compounds,[28–30] multidentate ligands[31–38] and *bridging* poly-monodentate oxazoline ligands in discreet polymetallic species,[33,36,39,40] cages[40,41] or coordination polymers[42–46] to impose a chiral environment around the metal atom. On the other hand, chiral *non-bridging* monodentate oxazoline complexes with non-covalent interactions are fairly unexplored,[47] especially monodentate oxazolines with axial or helical chirality.[47–49]

In this publication, using BOX ligands as an inspiration (Fig. 3, top), we have designed simple, *non-bridging* mono-oxazoline ligands capable of inducing helical chirality in supramolecular late transition metal complexes (Fig. 3, bottom).[50] In those complexes, we have incorporated a phenyl ring on the oxazoline C2-carbon atoms in order to facilitate aromatic stacking (see Fig. 3, top left, for the numbering scheme). Stereoselective formation of helically chiral tetrahedral metal complexes can be directed by introducing a bulky substituent on the oxazoline C4-carbon atom (Fig. 3, bottom). Additionally, we appended chiral amino acids to the *meta* position of the 2-phenyl ring to investigate the interplay between point chirality of amino acids and oxazolines on chirality transfer to the metal centre, *via* hydrogen bonding interactions, inspired by 1,*n*′-disubstituted ferrocene peptides (Fig. 2). We present herein, detailed crystallographic, spectroscopic, and computational studies.

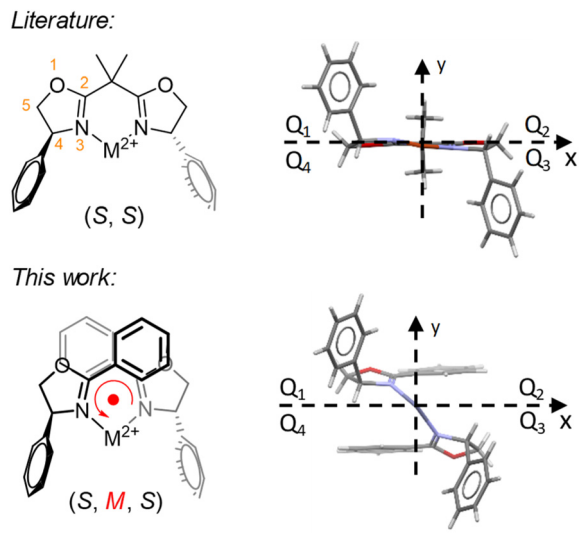

Fig. 3 A copper(II) BOX catalyst (top row)[34] and on the crystal structure of an (*M*)-helically chiral complex with monodentate oxazolines reported in this paper (bottom row). The red circle represents the axis of the helix. The oxazoline ring atom numbering is given on the structure in the first row (orange). Anions are omitted for clarity.

Results and discussion

Synthesis

A set of oxazoline ligands **1** with substituents of varying electron donating or withdrawing character, bulkiness and capability for non-covalent interactions on the 2-aryl group were synthesized (Scheme 1). In most cases, the R group is a 2-phenyl, with *para* ($\mathbf{1_H}$, $\mathbf{1_F}$ and $\mathbf{1_N}$) or *meta* ($\mathbf{1_{mA}}$, $\mathbf{1_{mA}}$*, $\mathbf{1_{m2A}}$ and $\mathbf{1_{m2A}}$*) substituents, except for ligand $\mathbf{1_p}$ which contains an unsubstituted polyaromatic 1-pyrene group instead. Ligands $\mathbf{1_{mA}}$, $\mathbf{1_{mA}}$*, $\mathbf{1_{m2A}}$ and $\mathbf{1_{m2A}}$* additionally contain either

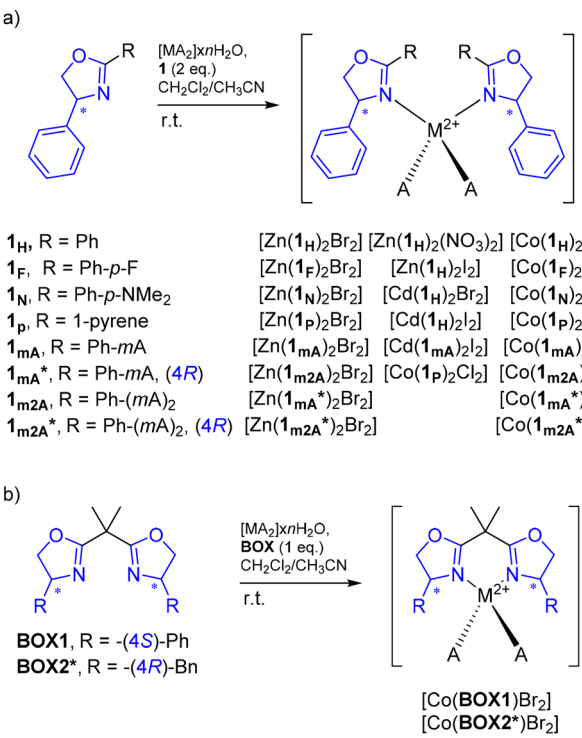

$\mathbf{1_H}$, R = Ph	$[Zn(\mathbf{1_H})_2Br_2]$	$[Zn(\mathbf{1_H})_2(NO_3)_2]$	$[Co(\mathbf{1_H})_2Br_2]$
$\mathbf{1_F}$, R = Ph-*p*-F	$[Zn(\mathbf{1_F})_2Br_2]$	$[Zn(\mathbf{1_H})_2I_2]$	$[Co(\mathbf{1_F})_2Br_2]$
$\mathbf{1_N}$, R = Ph-*p*-NMe_2	$[Zn(\mathbf{1_N})_2Br_2]$	$[Cd(\mathbf{1_H})_2Br_2]$	$[Co(\mathbf{1_N})_2Br_2]$
$\mathbf{1_p}$, R = 1-pyrene	$[Zn(\mathbf{1_P})_2Br_2]$	$[Cd(\mathbf{1_H})_2I_2]$	$[Co(\mathbf{1_P})_2Br_2]$
$\mathbf{1_{mA}}$, R = Ph-*m*A	$[Zn(\mathbf{1_{mA}})_2Br_2]$	$[Cd(\mathbf{1_{mA}})_2I_2]$	$[Co(\mathbf{1_{mA}})_2Br_2]$
$\mathbf{1_{mA}}$*, R = Ph-*m*A, (4*R*)	$[Zn(\mathbf{1_{m2A}})_2Br_2]$	$[Co(\mathbf{1_P})_2Cl_2]$	$[Co(\mathbf{1_{mA}})_2Br_2]$
$\mathbf{1_{m2A}}$, R = Ph-(*m*A)$_2$	$[Zn(\mathbf{1_{mA}}^*)_2Br_2]$		$[Co(\mathbf{1_{mA}}^*)_2Br_2]$
$\mathbf{1_{m2A}}$*, R = Ph-(*m*A)$_2$, (4*R*)	$[Zn(\mathbf{1_{m2A}}^*)_2Br_2]$		$[Co(\mathbf{1_{m2A}}^*)_2Br_2]$

Scheme 1 Reaction conditions: $[MA_2]$, M = Zn^{2+}, Cd^{2+} or Co^{2+}, A = Br^-, I^- or NO_3^-; CH_2Cl_2, r.t. The chirality at position 4 of the oxazoline ring is (*S*) in all cases except for ligands denoted with an asterisk (*), which contain (4*R*) chirality, additionally marked by "(4*R*)" in the scheme. All amino acid moieties are L-alanine methyl ester moieties *meta* substituted on the 2-phenyl group (*m*A).

one ($\mathbf{1_{mA}}$ and $\mathbf{1_{mA}}$*) or two ($\mathbf{1_{m2A}}$ and $\mathbf{1_{m2A}}$*) L-alanine methyl ester moieties (*m*A) with capacity for hydrogen bonding, (di) *meta* substituted on the 2-phenyl group. The ligands are derived from (*S*)-phenylglycinol, except when denoted by an asterisk ($\mathbf{1_{mA}}$* and $\mathbf{1_{m2A}}$*) indicating (*R*)-phenylglycinol. The oxazoline ligands $\mathbf{1_F}$, $\mathbf{1_N}$, $\mathbf{1_P}$, $\mathbf{1_{m2A}}$ and $\mathbf{1_{m2A}}$* were prepared in two steps with good yields according to previously reported procedures (Scheme 1, Schemes S1 and S2, Fig. S1a and S1b),[48,51] while ligands $\mathbf{1_H}$, $\mathbf{1_{mA}}$ and $\mathbf{1_{mA}}$* have been previously described.[48,49,52] All newly synthesized ligands have been characterized by NMR, UV-Vis, CD and IR spectroscopies, as well as HRMS spectrometry. For ligand $\mathbf{1_{mA}}$*, a single crystal structure was also obtained (Fig. S60).

A set of twenty-four zinc(II), cadmium(II) and cobalt(II) metal complexes were synthesized *in situ* by stirring the ligand and the metal precursor in a 2 : 1 ratio in CH_2Cl_2 or a CH_2Cl_2/CH_3CN mixture (Scheme 1a; scope overview is presented in Table S1, Fig. S1c, SI section 9). Metal precursors with various anions were used; namely, Cl^-, Br^-, I^-, NO_3^-, ClO_4^-, BF_4^- or $CF_3SO_3^-$. The syntheses were attempted first with ligands $\mathbf{1_H}$, $\mathbf{1_F}$, $\mathbf{1_N}$ and $\mathbf{1_P}$ while for ligands $\mathbf{1_{mA}}$, $\mathbf{1_{mA}}$*, $\mathbf{1_{m2A}}$ and $\mathbf{1_{m2A}}$* preparation of metal complexes was carried out only with $ZnBr_2$, CdI_2 and $CoBr_2$. Synthesis of cobalt(II) chloride derivatives revealed their poor solubility and stability in comparison to their bromide analogues. Cobalt(II) complexes of commercially available bisoxazoline ligands were synthesized for comparison (Scheme 1b).

Characterization in solid state

XRD-analysis. Preparation of single crystals of various zinc(II), cadmium(II) and cobalt(II) complexes with ligands $\mathbf{1_H}$, $\mathbf{1_F}$, $\mathbf{1_N}$, $\mathbf{1_P}$, $\mathbf{1_{mA}}$, $\mathbf{1_{mA}}$*, $\mathbf{1_{m2A}}$ and $\mathbf{1_{m2A}}$* has been attempted in order to study the influence of choice of metal, electron donating groups, non-covalent interactions and chiral centres on structural variation in solid state. All crystallized structures contain (4*S*)-phenyl oxazoline, while all attempts to grow suitable single crystals of (4*R*)-derivatives were unsuccessful. Eighteen single crystals of zinc(II), cadmium(II) or cobalt(II) metal complexes with oxazoline ligands have been obtained, two of which are bisoxazoline **BOX1** and **BOX2*** cobalt(II) complexes. Selected ORTEP diagrams[53] are highlighted in Fig. 4, while other ORTEP diagrams and crystal packings are shown in Fig. S50–S74; experimental data for the X-ray diffraction studies are listed in Tables S3–S7. Dihedral angles α (see Fig. S48a for definition), selected bond lengths and angles are collected in Table S2 (see SI section 9 and Fig. S48 and S49 for details).

Halide derivatives. All crystal structures of halide metal complexes are approximately C_2-symmetric and adopt a subtype IIa conformation with stacked 2-phenyl oxazolines in an offset, crossed fashion (Fig. 5, top left; see Fig. S49 for various possible geometries; Table S2), regardless of electron donating or steric nature of the substituent on the 2-aryl group, or cation and halide anion size. Additionally, 2-phenyl groups are the ends of a helix, in which the metal atom lays in the middle of

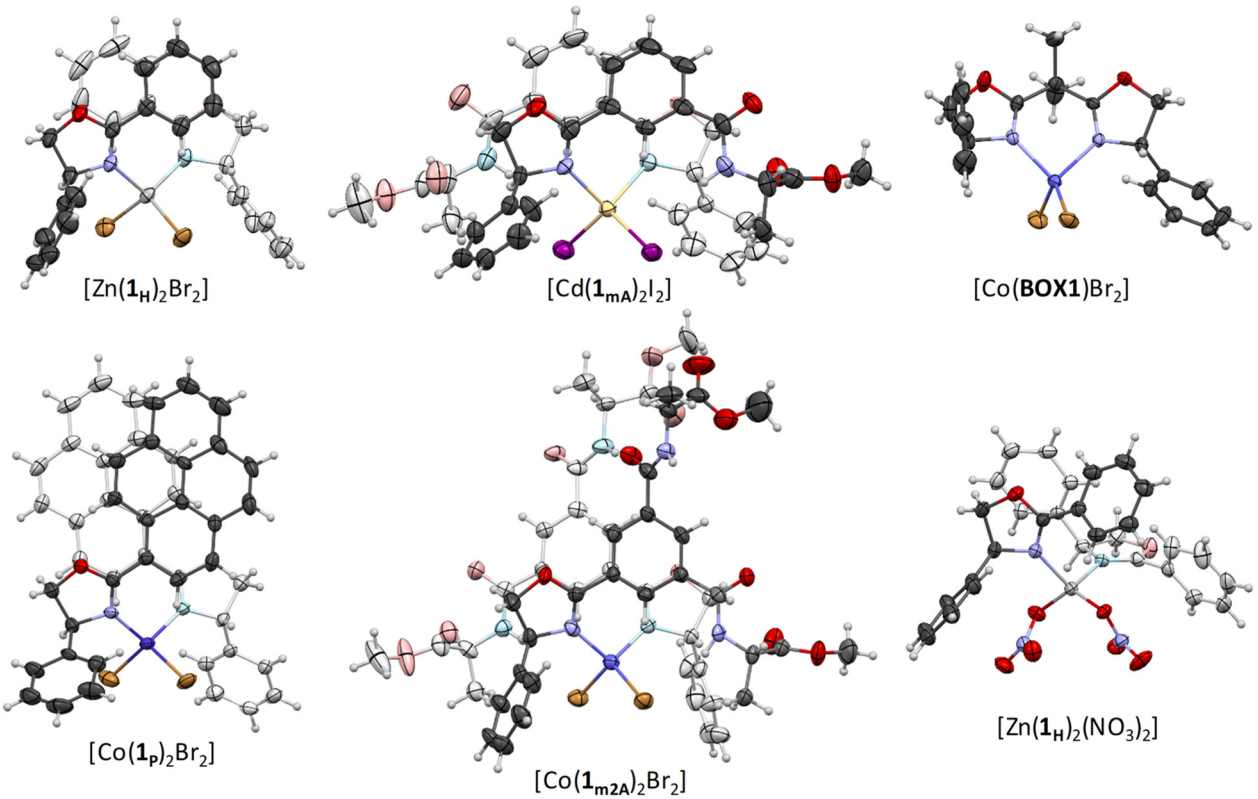

Fig. 4 ORTEP-III drawings[53] of complexes $[Zn(\mathbf{1_H})_2Br_2]$, $[Cd(\mathbf{1_{mA}})_2I_2]$, $[Co(\mathbf{BOX1})Br_2]$, $[Co(\mathbf{1_P})_2Br_2]$, $[Co(\mathbf{1_{m2A}})Br_2]$ and $[Zn(\mathbf{1_H})_2(NO_3)_2]$ with 30% ellipsoid probability level for SCXRD-determined structures.

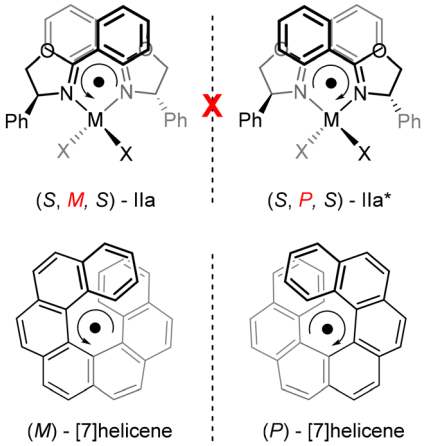

Fig. 5 Helical chirality determination in subtype IIa and IIa* geometries, see Fig. S49 for details. The black dots represent the axis of helicity. The two subtypes (*S*,*M*,*S*)-IIa and (*S*,*P*,*S*)-IIa* are diastereomeric for our complexes due to the incorporated (4*S*)-phenyl-containing chiral centers.

the helix backbone. In a similar way that helical chirality is determined for (*M*)- and (*P*)-[7]helicene, helical chirality (*M*) or (*P*) can be assigned to the subtype IIa conformation found in these crystal structures (Fig. 5). Similar geometries have been observed in crystal structures of zinc(II) halide complexes of achiral 2-phenyl oxazoline ligands, with (*M*)- and (*P*)-helicates evenly distributed among those structures.[54,55] In our case, greater steric hindrance in subtype IIa* (Fig. 5, right) is expected between the (4*S*)-phenyl of one ligand and 2-phenyl of the other ligand than in subtype IIa, facilitating IIa geometry formation with the (*M*)-helical chirality (see below in Computational analysis section). On the other hand, incorporation of a (4*R*)-substituent is expected to facilitate IIa* formation with (*P*)-helical chirality, which is consistent with the results of CD spectroscopy, see below. This premise is further corroborated by our previous results; ligand $\mathbf{1_{mA}}$* was used to prepare a rhodium(I) 1,5-cyclooctadiene complex, [Rh($\mathbf{1_{mA}}$*)$_2$COD]BF$_4$, for which a single crystal was obtained.[49] Although this is a square-planar Rh(I) complex, (*P*)-helical chirality could clearly be assigned to the complex.

Moreover, in the crystal structures of amino acid derivatives [Zn($\mathbf{1_{mA}}$)$_2$Br$_2$], [Cd($\mathbf{1_{mA}}$)$_2$I$_2$] and [Co($\mathbf{1_{mA}}$)$_2$Br$_2$], the amide hydrogen atoms of two alanine moieties were consistently found oriented towards halide anions (X···H–N), see Fig. 4, top middle for [Cd($\mathbf{1_{mA}}$)$_2$I$_2$]. Consistent occurrence of this conformer is contrary to the initial expectations that Herrick or van Staveren conformers would be obtained (see Fig. 2). In the case of complexes with four alanine moieties [Zn($\mathbf{1_{m2A}}$)$_2$Br$_2$] and [Co($\mathbf{1_{m2A}}$)$_2$Br$_2$], two alanine moieties form the X···H–N motif, while the other two interact *via* van Staveren hydrogen bonding,[23] see Fig. 4, bottom middle for [Co($\mathbf{1_{m2A}}$)$_2$Br$_2$]. In that structure, the adjacent complex molecules are infinitely stacked in an offset fashion in a way that those alanine moieties are also part of van Staveren hydrogen bonding with neighbouring molecules, forming infinite supramolecular polymeric chains in solid state. For all five crystal structures of alanine-containing metal complexes, the subtype IIa geometry with (*S*,*M*,*S*)-stereochemistry is retained.

Non-halide derivatives. Attempts to synthesize zinc, cadmium and cobalt non-halide metal complexes resulted in either amorphous, cotton-like fibrous or oily residues, or showed signs of degradation over time. From these mixtures, single crystals of unreacted metal precursors (cadmium) or ligands were isolated in multiple attempts, suggesting that coordination might not be occurring at these reaction conditions. However, a single crystal of a non-halide derivative [Zn($\mathbf{1_H}$)$_2$(NO$_3$)$_2$] was successfully obtained from a CH_2Cl_2 : CH_3CN : hexane = 2 : 1 : 3 solution at the edges of a fibrous-like solid after several weeks. In comparison to the halide analogues, the [Zn($\mathbf{1_H}$)$_2$(NO$_3$)$_2$] complex adopted a different type of arrangement of ligands within the complex in solid state (Fig. 4, bottom right).

Spectroscopic characterization in solution

NMR analysis. ^{1}H and ^{13}C NMR spectra were recorded for all synthesized ligands and all twelve diamagnetic metal complexes of Zn(II) and Cd(II). ^{1}H NMR spectra could be recorded in $CDCl_3$ for all ligands and most halide complexes, while for [Cd($\mathbf{1_H}$)$_2$Br$_2$] and [Zn($\mathbf{1_H}$)$_2$(NO$_3$)$_2$] CD_3CN and CD_3OD had to be used due to poor solubility at $c \approx 6$ mM in $CDCl_3$. NMR spectra of all studied complexes suggest C_2-symmetry of species present in solution.

All halide complexes show a downfield shift of the hydrogen atom attached to the chiral C4 oxazoline carbon atom upon complexation (by up to 0.83 ppm; SI sections 3 and 4). There is only one set of sharp peaks in ^{1}H NMR spectrum of the nitrate derivative in CD_3CN. In contrast, ligand peaks are broad in the spectra of halide metal complexes [M($\mathbf{1}$)$_2$X$_2$] of ligands $\mathbf{1_H}$, $\mathbf{1_F}$, $\mathbf{1_N}$, $\mathbf{1_P}$, $\mathbf{1_{mA}}$*, $\mathbf{1_{m2A}}$ and $\mathbf{1_{m2A}}$* recorded at room temperature, indicating that there might be more than one species in solution in equilibrium at room temperature. In order to confirm whether the peak broadening occurs due to a presence of both coordinated and non-coordinated ligands, ^{1}H NMR spectra of [Zn($\mathbf{1_H}$)$_2$Br$_2$], [Zn($\mathbf{1_N}$)$_2$Br$_2$], [Zn($\mathbf{1_P}$)$_2$Br$_2$] and [Zn($\mathbf{1_{m2A}}$)$_2$Br$_2$] in $CDCl_3$ were collected every 20 °C in a temperature range from −40 °C to 40 °C (Fig. 6, Fig. S2a and S3–S9). For [Zn($\mathbf{1_H}$)$_2$Br$_2$], [Zn($\mathbf{1_N}$)$_2$Br$_2$] and [Zn($\mathbf{1_P}$)$_2$Br$_2$] complexes, signals become sharper with decreasing temperature and there are no apparent changes in their chemical shifts, indicating that C_2-symmetry is also retained (Fig. 4, Fig. S2a and S3–S7). Spectra of metal complexes with alanine moieties show the presence of hydrogen bonding (Fig. 7), reflected in the downfield shift of the amide hydrogen atoms by more than 0.45 ppm for complexes of $\mathbf{1_{mA}}$ and 1.09 ppm for $\mathbf{1_{m2A}}$, as well as significant downfield shifts of the 2-phenyl aromatic signals (by up to 0.81 ppm). These results strongly indicate that complexation facilitates non-covalent interactions in solution. The NMR spectra of the [Zn($\mathbf{1_{m2A}}$)$_2$Br$_2$] complex at different temperatures were recorded as well (Fig. S8). Interestingly, an opposite trend of signal sharpening with temperature can be seen for oxazoline and alanine ^{1}H NMR peaks, *i.e.* oxazoline peaks sharpen with decreasing temperature, while alanine peaks

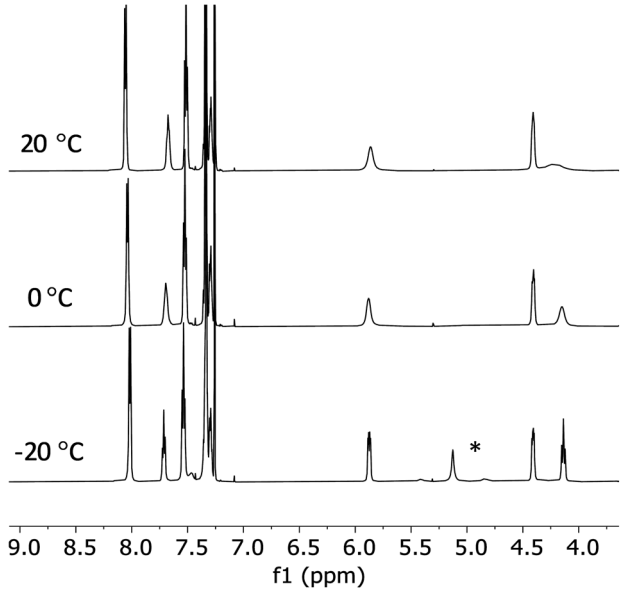

Fig. 6 ^{1}H NMR spectra of $[Zn(\mathbf{1_H})_2Br_2]$ in $CDCl_3$ at 20 °C, 0 °C and −20 °C, c = 6 mM. The signal denoted by an asterisk most likely corresponds to a protonated species (for a detailed analysis see discussion and Fig. S2a–f in the SI).

broaden with decreasing temperature, especially the alanine amide signals. These changes suggest that amides may be involved in different hydrogen bonding motifs (*e.g.* Herrick or van Staveren) which are averaged at room temperature.

UV-Vis and CD spectroscopy. For all ligands and most halide complexes, UV-Vis and CD spectra could be recorded in CH_2Cl_2, while for $[Cd(\mathbf{1_H})_2Br_2]$ and $[Zn(\mathbf{1_H})_2(NO_3)_2]$ CD_3CN and CD_3OD had to be used due to lower solubility (SI section 5). Spectra of ligands and complexes indicate that complexation occurred (Fig. 8, top left; SI section 5b, Fig. S18–S26). For comparison, zinc and cadmium complexes of ligand $\mathbf{1_H}$ were also recorded in acetonitrile. Both UV-Vis and CD spectra of studied ligands and corresponding complexes in CH_3CN share similar features, albeit with slightly different intensities, except for $[Zn(\mathbf{1_H})_2(NO_3)_2]$ and $[Cd(\mathbf{1_H})_2Br_2]$ (Fig. S27–S30).

For all studied cobalt complexes the induction of chirality around the metal atom was confirmed by the appearance of strong peaks in the visible region of the CD spectra. To further study the influence of ligand substituents on spectra of their metal complexes, UV-Vis and CD spectra of cobalt(II) derivatives were recorded in concentration range 0.015–2.775 mM (SI section 5c, Fig. S31–S46). Additionally, concentration experiments have been performed for all cobalt complexes. The results show linear dependency in all cases, indicating that there is no occurrence of additional aggregation or dissociation for these compounds at the studied conditions. The description of the CD results reported below is qualitative; the detailed understanding of the chirality transfer mechanism is difficult due to a subtle interplay of electronic, steric and stereochemical influences in C_2-symmetric metal complexes with monodentate ligands containing non-covalent interactions between them.[50] A UV-Vis spectrum and a crystal structure of a similar cobalt(II) complex has been reported in litera-

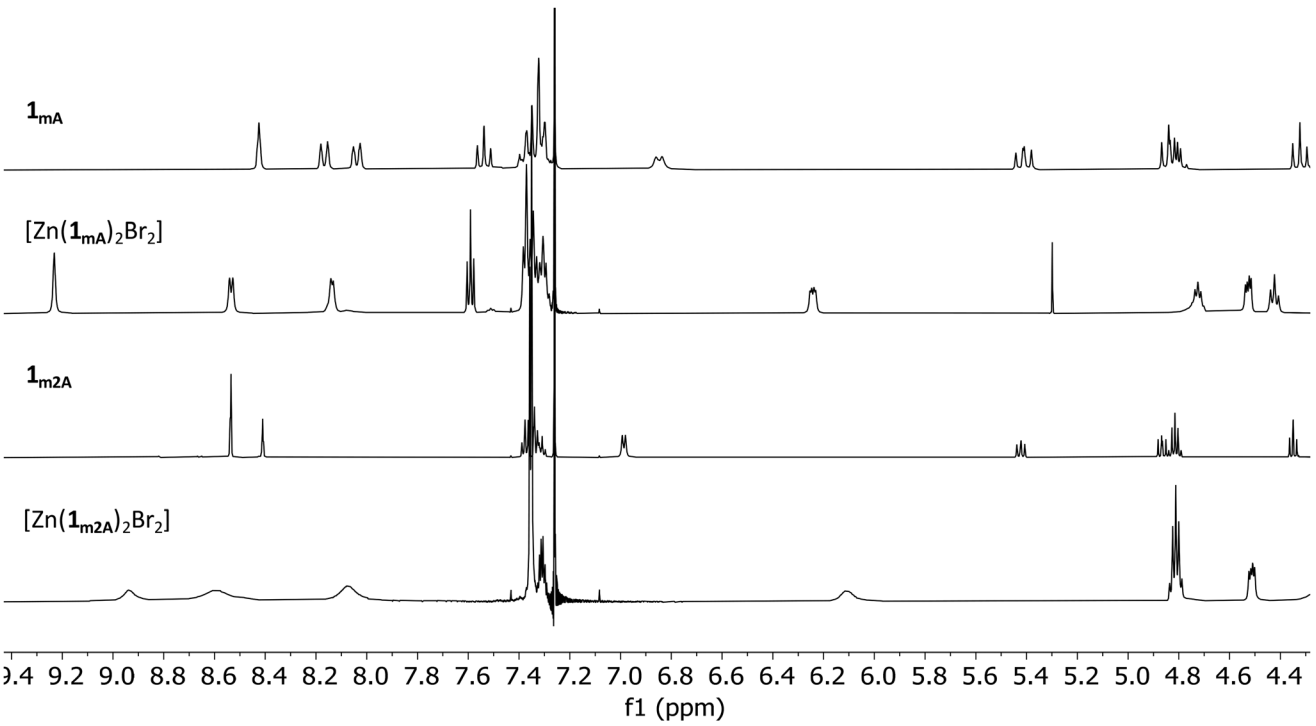

Fig. 7 ^{1}H NMR spectra of $\mathbf{1_{mA}}$, $[Zn(\mathbf{1_{mA}})_2Br_2]$, $\mathbf{1_{m2A}}$ and $[Zn(\mathbf{1_{m2A}})_2Br_2]$ in $CDCl_3$.

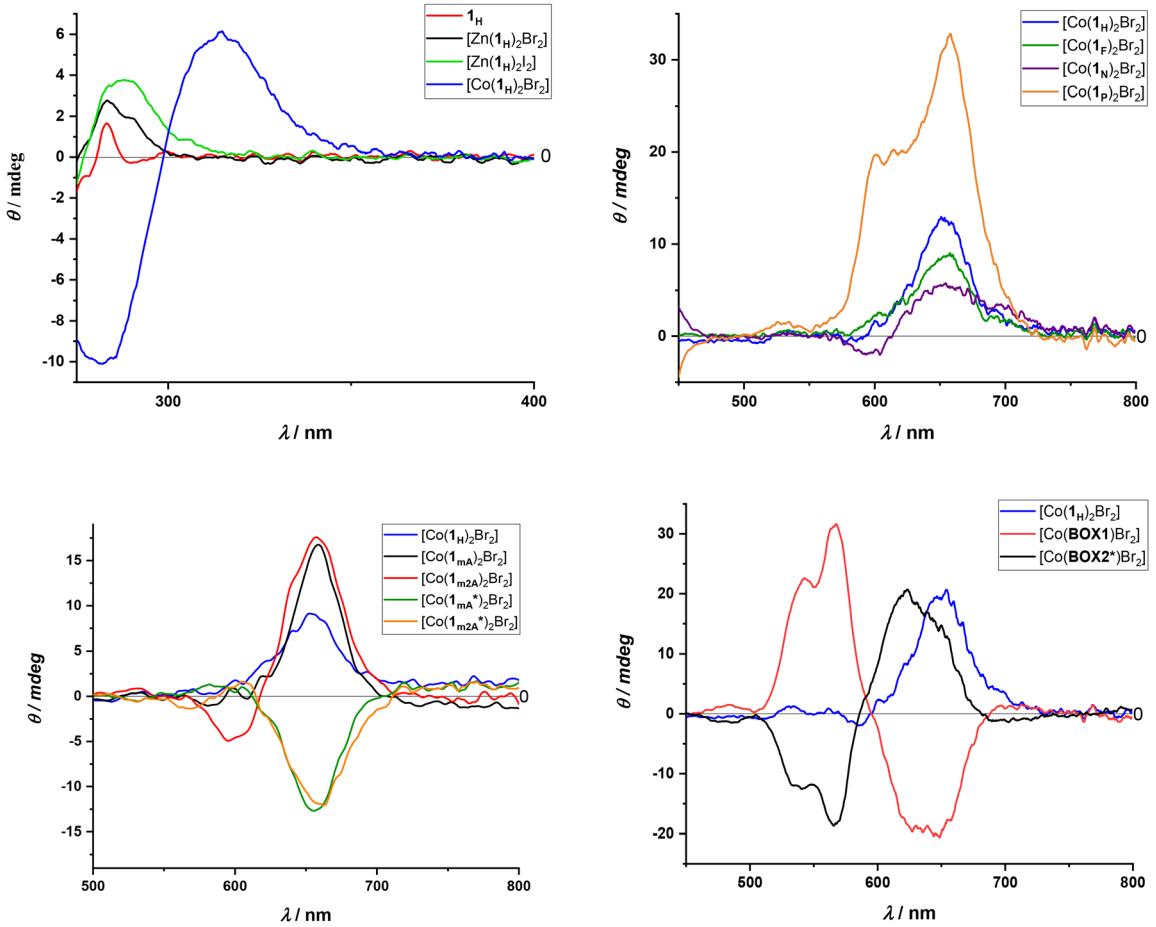

Fig. 8 Overlapped CD spectra in CH_2Cl_2 of: ligand $\mathbf{1_H}$ and corresponding zinc(II) and cobalt(II) halide complexes at c = 0.075 mM (top left); cobalt(II) bromide complexes of ligands $\mathbf{1_H}$, $\mathbf{1_F}$, $\mathbf{1_N}$ and $\mathbf{1_P}$ in the visible region of the spectrum at c = 1.13 mM (top right); cobalt(II) bromide complexes of ligands $\mathbf{1_H}$, $\mathbf{1_{mA}}$, $\mathbf{1_{mA}}$*, $\mathbf{1_{m2A}}$ and $\mathbf{1_{m2A}}$* in the visible region of the spectrum at c = 0.74 mM (bottom left); and cobalt(II) bromide complexes at c = 2.25 mM with ligands $\mathbf{1_H}$, (−)-2,2′-isopropylidenebis[(4*S*)-4-phenyl-2-oxazoline] (**BOX1**) and (+)-2,2′-isopropylidenebis[(4*R*)-4-benzyl-2-oxazoline] (**BOX2***) (bottom right).

ture with an achiral 2-(*p*-ethoxyphenyl)oxazoline ligand.[56] Apart from the characteristic cobalt(II) peak position at around 650 nm, the spectrum is largely incomparable with that of our compounds.

CD results for monodentate non-alanine cobalt complexes show minor differences for complex analogues bearing *para* substituted 2-phenyl groups ($\mathbf{1_H}$, $\mathbf{1_F}$ and $\mathbf{1_N}$ complexes), while differences are more pronounced for the more diverse pyrene $\mathbf{1_P}$ analogue. Inclusion of chiral alanine substituents further reveals interesting effects as well. The ellipticity values of the $\mathbf{1_{mA}}$ and $\mathbf{1_{mA}}$* derivatives indicate that the main contribution to the induction of chirality is imparted by the influence of the oxazoline C4 chiral centres. The signals at around 653 nm in the CD spectra of $\mathbf{1_{mA}}$ and $\mathbf{1_{m2A}}$ complexes, as well as $\mathbf{1_{mA}}$* and $\mathbf{1_{m2A}}$* complexes, are very similar in intensity and profile (Fig. 8, bottom left). This suggests that the inclusion of a second amino acid chain has no apparent influence on the chiral induction around the metal atom at the given conditions. The only exception is the appearance of a minimum at 594 nm for the $\mathbf{1_{m2A}}$ derivative. The intensities of the $\mathbf{1_{mA}}$ and $\mathbf{1_{m2A}}$ pair are larger by roughly two times in comparison to the $\mathbf{1_H}$ derivative, while the $\mathbf{1_{mA}}$* and $\mathbf{1_{m2A}}$* pair feature a peak at the same wavelength as the (*S*)-variants, but of the opposite sign. This suggests that the $\mathbf{1_{mA}}$ and $\mathbf{1_{m2A}}$ derivatives provide a more defined and rigid chiral structure around the metal atom, which we attribute to stronger non-covalent intramolecular interactions of the more suitable diastereoisomeric 4*S*/L combination of chiral centres in the ligand (see the Computational analysis section).

For further analysis, CD spectra have been recorded in the Vis region in CH_2Cl_2 at c = 2.25 mM of two cobalt complexes of commercially available bisoxazoline ligands, 2,2′-isopropylidenebis[(4*S*)-4-phenyl-2-oxazoline] (**BOX1**) and (+)-2,2′-isopropylidenebis[(4*R*)-4-benzyl-2-oxazoline] (**BOX2***) (Fig. 8, bottom right; Fig. S47). While the bisoxazoline complexes exhibit strong peaks in the 500–600 nm region, the monodentate derivative barely shows peaks in this region, with intensities lower by one order of magnitude. This could be explained by the difference in rigidity of bisoxazoline and mono-oxazoline complexes, where it is expected that mono-oxazoline

ligands have a less defined chiral environment around the metal due to greater conformational freedom (see Fig. S48 and S49). However, we were surprised to find that compound [Co(**BOX1**)Br_2] features a broad peak of the opposite sign with equal intensity as the $\mathbf{1_H}$ derivative, despite ligands **BOX1** and $\mathbf{1_H}$ both having (4*S*)-phenyl substituents. We show herein that in halide mono-oxazoline complexes the (4*S*)-substituents facilitate preferential formation of a conformation which features an additional chiral element, (*M*)-helicity, which directly involves the 2-phenyl groups and the metal atom (see the Characterization in solid state and Computational analysis sections).

Computational analysis

In order to further investigate the preferential tetrahedral geometries of monodentate oxazoline metal complex derivatives found in the solid state and in solution, we proceeded with the computational analysis. The studied conformations corresponded to types II–IV and subtypes a–d (Fig. S48 and S49) of zinc(II) and cobalt(II) bromide complexes with $\mathbf{1_H}$, $\mathbf{1_F}$, $\mathbf{1_N}$, $\mathbf{1_P}$, $\mathbf{1_{mA}}$*, $\mathbf{1_{m2A}}$ and $\mathbf{1_{m2A}}$* ligands as well as [Zn($\mathbf{1_H}$)$_2$(NO_3)$_2$]. All the relevant identified conformers were optimised using DFT calculation, and their total Gibbs free energies of DFT calculated conformers were used to help identify dominant species present in solution (chloroform or acetonitrile). Since the geometries of a tetrahedral cobalt complex were considered, the high-spin system was modelled. In all the studied complexes, the ligands coordinated the metal atom through the oxazoline nitrogen atoms, accurately reproducing the experimentally observed structures.

Non-alanine derivatives. The comparison of parameters of crystal structures and the most similar calculated conformers is given in Table 1.

The most stable conformer for each of the considered halide complexes was consistently found to be subtype IIa(1) with (*S*,*M*,*S*)-stereochemistry (Tables S8–S10 and S12), which fully agrees with the obtained crystal structures, regardless of the cation, electron-donating nature of the R group or of the used medium (with or without SMD solvation models). Moreover, for the halide complexes, a single conformer is clearly favoured in solution, with all the others being at least 2 kcal mol^{-1} less stable and thus negligible in population. Conversely, the nitrate derivative exhibited a greater number of conformers, many of which lie within the 2 kcal mol^{-1} window, with the effect particularly pronounced in acetonitrile. This is reflected in the values of the calculated probability (P_i) according to the Boltzmann distribution within the group of obtained conformers, indicating that the nitrate complex can assume different geometries across all three media (vacuum, $CHCl_3$, CH_3CN; Table S11). Furthermore, conformer (IIId1), which most closely matches the crystal structure of [Zn($\mathbf{1_H}$)$_2$(NO_3)$_2$], was not found to be the most stable in vacuum, $CHCl_3$ or CH_3CN.

In order to further investigate expected stability differences of (*S*,*M*,*S*)-IIa and (*S*,*P*,*S*)-IIa* diastereoisomers, corresponding zinc(II) bromide complex geometries with ligand $\mathbf{1_E}$, which is simply ligand $\mathbf{1_H}$ without the (4*S*)-phenyl substituent (also found in the crystal structure with the CCDC code ETUVIY),[54] and ligand $\mathbf{1_H}$ were calculated (Table S13). As expected, optimized (*S*,*M*,*S*)-IIa and (*S*,*P*,*S*)-IIa* conformations are equivalent for complex [Zn($\mathbf{1_E}$)$_2$$Br_2$]. For complex [Zn($\mathbf{1_H}$)$_2$$Br_2$], diastereoisomer (*S*,*M*,*S*)-IIa is more stable than (*S*,*P*,*S*)-IIa* by 8.5 kcal mol^{-1}. Obviously, the steric hindrance incurred by the (4*S*)-phenyl group drastically destabilizes the latter conformation. This finding is in agreement with the experimentally obtained, strictly subtype IIa halide crystal structures.

Table 1 Comparison of experimental and calculated dihedral angles α (see definition on Fig. S48a), in obtained crystal structures and calculated conformers of oxazoline metal complexes. All calculated values were given for conformers optimized in vacuum. For more details, see Tables S8–S12

Metal complex	α_1, α_2 (°)	Type	P_i [a]/%
Exp.[Zn($\mathbf{1_H}$)$_2$$Br_2$]	324.27, 338.83	IIa	—
Calc.[Zn($\mathbf{1_H}$)$_2$$Br_2$]	329.59, 329.59	IIa	99
Exp.[Zn($\mathbf{1_H}$)$_2$(NO_3)$_2$]	128.96, 303.44	IVa	—
Calc.[Zn($\mathbf{1_H}$)$_2$(NO_3)$_2$]	103.23, 260.22	IVa2	16
Calc.[Zn($\mathbf{1_H}$)$_2$(NO_3)$_2$]	175.41, 305.37	IIId1	1
Calc.[Zn($\mathbf{1_H}$)$_2$(NO_3)$_2$]	329.16, 329.17	IIa	63
Exp.[Zn($\mathbf{1_F}$)$_2$$Br_2$] [b]	325.67, 333.93	IIa	—
Calc.[Zn($\mathbf{1_F}$)$_2$$Br_2$]	329.32, 329.58	IIa	>99
Exp.[Zn($\mathbf{1_N}$)$_2$$Br_2$] [b]	334.43, 336.71	IIa	—
Calc.[Zn($\mathbf{1_N}$)$_2$$Br_2$]	330.44, 330.44	IIa	98
Exp.[Co($\mathbf{1_H}$)$_2$$Br_2$]	339.12, 323.35	IIa	—
Calc.[Co($\mathbf{1_H}$)$_2$$Br_2$]	333.3, 333.31	IIa	>99

[a] P_i is the probability that the complex molecule will have the given geometry within the calculated ensemble of conformers according to Boltzmann distribution. [b] Experimental angle values for independent complex molecules in the crystal lattice were averaged.

Alanine derivatives

Alanine-derivatives for the zinc bromide complexes [Zn($\mathbf{1}$)$_2$$Br_2$] include pairs of diastereomeric ligands $\mathbf{1_{mA}}$ and $\mathbf{1_{mA}}$*, as well as $\mathbf{1_{m2A}}$ and $\mathbf{1_{m2A}}$* (Scheme 1). Introduction of alanine moieties to the ligand structure increased its potential supramolecular interactions, particularly pronounced for the derivatives containing two alanine moieties. To focus on the most relevant structures, high-energy conformers were discarded before DFT optimization. The lowest-energy conformers of the diastereomeric pairs $\mathbf{1_{mA}}$/$\mathbf{1_{mA}}$* and $\mathbf{1_{m2A}}$/$\mathbf{1_{m2A}}$*, along with their relative Gibbs free energies, are shown in Fig. 9. Comprehensive data on relative Gibbs energies and non-covalent interactions for all conformers are provided in Tables S14–S17. Most of the optimized conformers for the four different complexes adopt the IIa geometry, with variations between the conformations mainly in the stacking of the 2-phenyl groups and the hydrogen-bonding motifs of the alanine substituents (Fig. 9, Fig. S75, Tables S14–S17). The lowest-energy conformers of each complex are approximately of C_2-symmetry.

For the pair of diastereomeric ligands having a single alanine moiety, the geometry of the most stable conformer differs. The most stable conformer for [Zn($\mathbf{1_{mA}}$)$_2$$Br_2$] complex shows two Br···H–N hydrogen bonds, with no additional interactions between the alanine moieties. In addition, a few low-

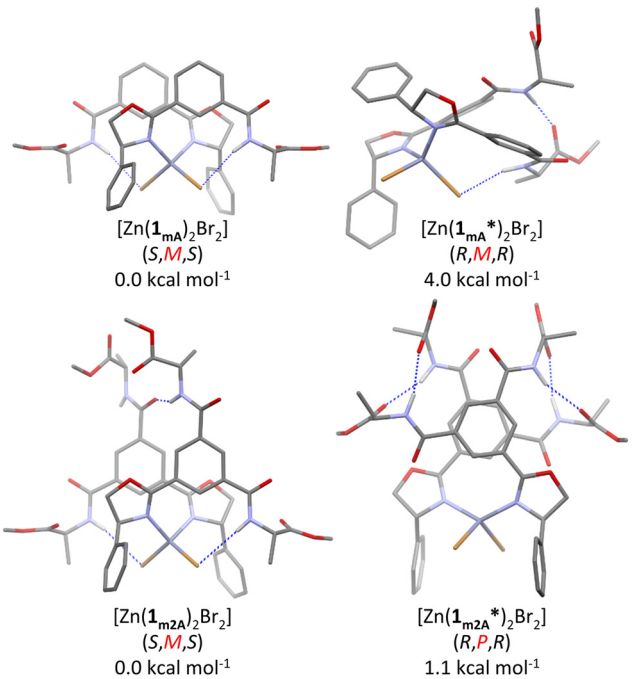

Fig. 9 Calculated structures of the most stable conformers of zinc bromide complexes with ligands $\mathbf{1_{mA}}$, $\mathbf{1_{mA}}$*, $\mathbf{1_{m2A}}$ and $\mathbf{1_{m2A}}$*. Relative Gibbs energies (ΔG) denoted below structures are calculated for diastereomeric pairs $\mathbf{1_{mA}}$ and $\mathbf{1_{mA}}$*, as well as $\mathbf{1_{m2A}}$ and $\mathbf{1_{m2A}}$*, respectively. All hydrogen atoms, except for those interacting *via* hydrogen bonding, were removed for clarity. Hydrogen bonds are highlighted by blue, dashed lines.

lying conformers retain the Br···H–N interaction, and due to the appearance of no additional hydrogen bonds between the ligands, the coordination of bromides with the amide group seems to restrict the conformational flexibility of the ligand. In contrast, a conformer lacking these interactions is flexible enough so that the hydrogen bonding between the alanine moieties can be achieved through the formation of either van Staveren or Herrick moieties. Still, those conformers are ~10 kcal mol^{-1} less stable than the minimum. On the other hand, for the most stable conformer of [Zn($\mathbf{1_{mA}}$*)$_2$Br$_2$] complex only one Br···H–N interaction is present. In addition, a single semi-Herrick type N–H···O hydrogen bond is formed between the two alanine moieties (see Fig. S75 for details).

As mentioned, the addition of the second alanine moiety leads to an increase in the number of hydrogen bond donors and acceptors, therefore opening the possibility of extensive hydrogen bonding between the two ligands within each complex. The most stable conformer for [Zn($\mathbf{1_{m2A}}$)$_2$Br$_2$] complex still adopts the two Br···H–N hydrogen bonds as was the case of $\mathbf{1_{mA}}$, but also an additional van Staveren O···H–N hydrogen bond between the alanine moieties. In other conformers of this complex, the loss of Br···H–N interactions is accompanied by the formation of additional Herrick and van Staveren hydrogen bonds, but this results in higher relative Gibbs free energies. For [Zn($\mathbf{1_{m2A}}$*)$_2$Br$_2$] complexes, the most stable conformer features two Herrick hydrogen-bonding motifs. Higher energy conformers feature different combinations of van Staveren or semi-Herrick types of hydrogen bonding, but still show a lower total number of hydrogen bonds as compared to the most stable one. For [Zn($\mathbf{1_{m2A}}$*)$_2$Br$_2$], coordination of bromides by the Br···H–N was noticed, but the energy of that conformer is ~10 kcal mol^{-1} less stable than the minimum.

Compared to the crystal structures of $\mathbf{1_{mA}}$, $\mathbf{1_{mA}}$* and $\mathbf{1_{m2A}}$ zinc bromide complexes, the most stable conformers derived computationally reproduce those structures well for both systems, indicating both the validity of the computational approach as well as showing that the geometry of the crystal structures corresponds to the most thermodynamically stable conformer present in solution. Together, these results indicate that a set configuration of stereocenters within a ligand influences the spatial arrangement within the complex and contributes to the overall stability of the complex since it directly affects the possibility of forming additional stabilizing non-covalent interactions.

These results suggest a possible match/mismatch effect between the oxazoline 4*R*/4*S* and alanine L/D chiralities, in relation to the ability of diastereomers to maximize the stabilization by non-covalent interactions. This idea is further supported by an analysis of all structures exhibiting Herrick hydrogen bonding in the CSD database. Among 91 crystal structures (Table S18) with any amino acid configuration, compounds containing L-amino acids consistently adopt the Herrick A conformation (Fig. 10, left), whereas those with D-amino acids adopt the Herrick B conformation. For our case, if the IIa and IIa* placements of the oxazoline rings represent the preferred

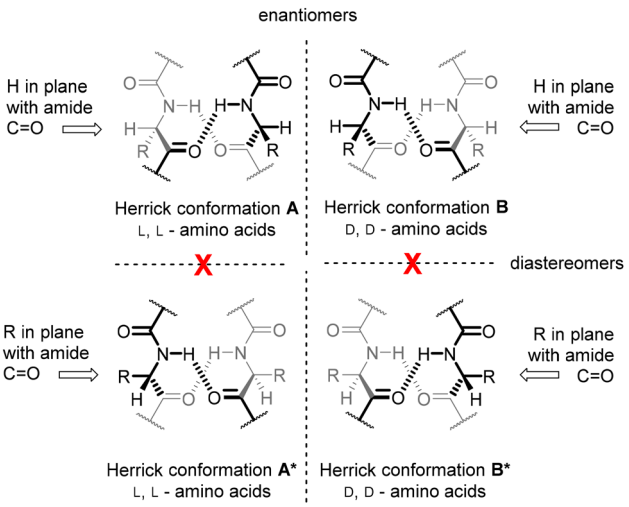

Fig. 10 Two possible conformations for Herrick hydrogen bonding between two amino acids is shown; Herrick conformations **A** and **A*** for L,L-amino acids and Herrick conformations **B** and **B*** for D,D-amino acids. The **A**/**B** structures have the α-hydrogen atom in plane with the amide carbonyl group, while the **A***/**B*** structures have the α-alkyl group R in plane with the amide carbonyl group. The **A**/**B** and **A***/**B*** pairs are enantiomeric, while **A**/**A*** and **B**/**B*** pairs are diastereomeric.

conformations, then the amino acid chains cannot adopt this arrangement for all combinations of (4*R*/4*S*)-oxazoline and L/D amino acid chirality. This is evident when comparing the crystal structure geometries with the calculated Herrick hydrogen-bonded geometries (Fig. 9, Tables S14–S17). The analysis indicates that the (4*R*)-oxazoline/L-Ala combination cannot achieve the same non-covalent interactions or bonding strength as the (4*S*)-oxazoline/L-Ala complexes, leading to a slightly less well-defined chiral environment around the metal centre. On the other hand, Herrick hydrogen bonding motifs are expected to be more favourable for the (4*R*)-oxazoline/L-Ala combination, as this arrangement allows a more favourable spatial orientation of the amino acid chains.

Conclusions

Twenty-four new chiral metal complexes were prepared from a set of ten chiral oxazoline ligands and characterized by NMR, UV-Vis, CD, IR and powder diffraction measurements. Single crystals suitable for diffraction measurements of 18 metal complexes were obtained; all obtained halide complexes of (4*S*)-phenyl monodentate oxazolines formed analogous (*M*)-helical structures, while the nitrate derivative adopted a different structure. NMR spectra confirm that complexation in solution occurs and indicate C_2-symmetry of the species in solution. Additionally, significant chemical shift changes in ^{1}H NMR spectra can be observed due to hydrogen bonding and aromatic stacking in the spectra of amino acid derivatives. UV-Vis and CD spectroscopy confirm complexation and induction of chirality around the metal atom. DFT results for non-alanine (4*S*)-phenyl derivatives showed that halide metal complexes bearing (*S*,*M*,*S*)-chirality are expected to be significantly more stable than the (*S*,*P*,*S*)-isomers at the calculated level of theory, regardless of the vacuum or solvent environment used. On the other hand, results for alanine-derivatives showed the importance of the matching/mismatching effect of chiral configurations on position 4 of the oxazoline ring and the amino acid substituents, where the 4*S*/L combination of point chiralities gave relatively more stable structures.

Previously, we have reported on induction of chirality in ferrocene dipeptide compounds (Fig. 11a)[23] and octahedral complexes with amino acid tridentate ligands (Fig. 11b).[57] Herein, we report on chiral induction in tetrahedral metal complexes. *I.e.*, we have shown that incorporating (*S*)-chirality on C4 carbon atom of the 2-aryloxazoline ring facilitates preferential formation of IIa conformation, consequently inducing (*M*)-helical chirality around the metal atom. This is a first report on preparation of helicates bearing simple, non-bridging monodentate oxazoline ligands in tetrahedral complexes. Furthermore, we have demonstrated how the structural variations influence the chirality around the metal atom, in particular, the variation of the achiral 2-aryl substituents or the inclusion of the chiral alanine amino acid substituents. These results offer a tool for reliable construction of simple, helically chiral, supramolecular tetrahedral metal complexes of 2-aryl-

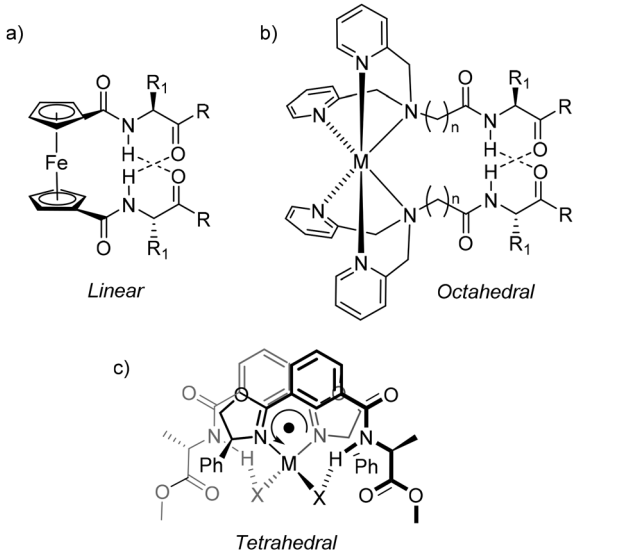

Fig. 11 Induction of chirality in: (a) dipeptidic ferrocene compounds,[21] (b) octahedral metal complexes of peptidic tridentate ligands[66] and (c) tetrahedral metal complexes of monodentate 2-aryloxazoline ligands presented herein.

oxazolines, which may further be functionalized to serve specific applications.

Experimental

General remarks

Reactions were carried out in ordinary glassware and chemicals were used as purchased from commercial suppliers without further purification. Pure L-amino acid methyl esters and amino acid-derived amino alcohols were used in all syntheses unless stated otherwise. Reactions were monitored by TLC on silica gel 60 F_{254} plates and detected with a UV lamp (254 nm); crude products were purified using classic column or *flash* chromatography. **ESI mass spectra** were recorded on a HPLC-MS system (Agilent Technologies 1200) coupled with a 6410 Triple-Quadrupole mass spectrometer, operating in a positive ESI mode. **High-resolution mass spectra** were obtained on a MALDI TOF-TOF instrument using a CHCA matrix. **NMR spectra** were obtained on a Bruker Avance 300 or 600 spectrometer, operating at 300 or 600 MHz for ^{1}H and 75 or 150 MHz for ^{13}C; if not indicated further the spectra were recorded at room temperature. Chemical shifts, δ (ppm), indicate a downfield shift from the internal standard, tetramethylsilane, TMS. Coupling constants, *J*, are given in Hz. Individual peaks are marked as: singlet (s), doublet (d), triplet (t), quartet (q), quintet (quin.) or multiplet (m). **UV-Vis spectra** were recorded on *Cary* 100 spectrophotometer and **CD spectra** were recorded on *Jasco* J-815 spectropolarimeter in 1.0 cm quartz Suprasil cells. Stock solutions of the isolated compounds were prepared for UV-Vis and CD measurements. The measured absorbance *A* (in UV-Vis) is converted to concentration-independent ε [M^{-1}

cm^{-1}] through the Lambert–Beer equation. The measured ellipticity θ [°] (in CD) is converted into the concentration independent $\Delta\varepsilon$ [M^{-1} cm^{-1}] through the relation $\Delta\varepsilon = \theta/(b \times 32\,982 \times c)$, where b [cm] is the path length and c [M] is the concentration. **IR spectra** were recorded in solid state, using an ATR Agilent Cary 630 FT-IR spectrometer in the 4000–600 cm^{-1} (ATR) region. **X-ray powder diffraction** measurements were performed using PANalytical Aeris instrument, with measurement parameters: Bragg–Brentano geometry (θ–2θ), source of radiation: Cu Kα (λ = 1.54184 Å), measured from 5° to 50° at 5.2° per minute.

Ligands $\mathbf{1_{mA}}$ and $\mathbf{1_{mA}}$* have been prepared according to their previously reported synthetic procedures and the collected spectra correspond to previously reported results.[48,49]

General peptide coupling to mono-carboxylic acids procedure

Carboxylic acid (1 equivalent) was dissolved in CH_2Cl_2 (100 mL). Peptide coupling reagent, TBTU/HOBt, (1 equivalent) and DIPEA (4 equivalents) were added and stirring was continued for 60 min at room temperature (HATU). An amino alcohol (1 equivalent) was added and stirring was continued for 24 hours. The reaction mixture was washed with $NaHCO_3$ (sat. aq., 3 × 100 ml), citric acid (10% aq., 3 × 100 mL) and NaCl (sat. aq. 100 mL). The organic phase was dried over $NaSO_4$, filtered and evaporated under reduced pressure to yield the crude product.

General one-pot coupling to di- and tri-carboxylic acids procedure in DCM

Isophthalic or trimesic acid (2 equivalents) was dissolved in DCM (100 mL). Peptide coupling reagent (HATU, 3 equivalents) and DIPEA (10 equivalents) were added and stirring was continued for 60 min at room temperature. An amino acid hydrochloride (3.1 equivalents) was added in small portions and stirring was continued for 24 hours. Then, a peptide coupling reagent (HATU, 3.6 equivalents) and DIPEA (14.4 equivalents) were added and stirring was continued for 60 min at room temperature (TBTU/HOBt, HATU). An amino alcohol (3.1 equivalents) was added in small portions and stirring was continued for 24 hours. The reaction mixture was washed with $NaHCO_3$ (sat. aq., 3 × 100 ml), citric acid (10% aq., 3 × 100 mL) and NaCl (sat. aq., 100 mL). The organic phase was dried over Na_2SO_4, filtered and evaporated under reduced pressure to yield the crude product.

$Phg^{\#}$–C_6H_5. Benzoic acid (2.0 mmol, 244.2 mg), TBTU (2.0 mmol, 642.2 mg), HOBt (2.0 mmol, 306.2 mg), (*S*)-phenylglycinol ($Phg^{\#}$, 2.0 mmol, 274.4 mg), DIPEA (8 mmol, 1.394 mL). *Flash* chromatography, prepacked silicagel column, 3% CH_3OH in CH_2Cl_2. Yield 465.7 mg (1.93 mmol, 97%), colorless oil. $M_r(C_{15}H_{15}NO_2)$ = 241.11. ESI-MS (*m*/*z*): 242.15 (M + H^+, 99%), 264.10 (M + Na^+, 53%), 505.15 (2M + Na^+, 100%). ^{1}H NMR (600 MHz, $CDCl_3$) δ/ppm: 7.84–7.80 (m, 2H), 7.56–7.30 (m, 8H), 6.82 (s, 1H), 5.33–5.26 (m, 1H), 4.03 (m, 2H). ^{13}C NMR (151 MHz, CD_3OD) δ/ppm: 170.36, 141.40, 135.85, 132.68, 129.53, 129.52, 128.45, 128.42, 128.03, 66.05, 57.79.

$Phg^{\#}$–*p*C_6H_4–F. *p*-Fluorobenzoic acid (2.0 mmol, 280.2 mg), TBTU (2.0 mmol, 642.2 mg), HOBt (2.0 mmol, 306.2 mg), (*S*)-phenylglycinol ($Phg^{\#}$, 2.0 mmol, 274.4 mg), DIPEA (8 mmol, 1.394 mL). *Flash* chromatography, prepacked silicagel column, 3% CH_3OH in CH_2Cl_2. Yield: 447.0 mg (1.73 mmol, 86%), white solid. $M_r(C_{15}H_{14}FNO_2)$ = 259.10. ESI-MS (*m*/*z*): 260.10 (M + H^+, 100%), 282.20 (M + Na^+, 71%), 541.15 (2M + Na^+, 41%). ^{1}H NMR (600 MHz, $CDCl_3$) δ/ppm: 7.86–7.81 (m, 2H), 7.44–7.30 (m, 5H), 7.18–7.07 (m, 2H), 6.77 (s, 1H), 5.27 (dt, *J* = 7.2, 4.7 Hz, 1H), 4.02 (s, 2H). ^{13}C NMR (151 MHz, CD_3OD) δ/ppm: 169.15, 167.02, 165.37, 141.33, 132.18, 132.16, 131.10, 131.04, 129.52, 128.45, 128.05, 128.02, 116.39, 116.25, 66.01, 57.85.

$Phg^{\#}$–*p*C_6H_4–NMe_2. *p*-(*N*,*N*-Dimethylamino) benzoic acid (2.0 mmol, 330.4 mg), TBTU (2.0 mmol, 642.2 mg), HOBt (2.0 mmol, 306.2 mg), (*S*)-phenylglycinol ($Phg^{\#}$, 2.0 mmol, 274.4 mg), DIPEA (8 mmol, 1.394 mL). *Flash* chromatography, prepacked silicagel column, 3% CH_3OH in CH_2Cl_2. Yield: 470.6 mg (1.7 mmol, 82%), white solid. $M_r(C_{17}H_{20}N_2O_2)$ = 284.15. ESI-MS (*m*/*z*): 285.11 (M + H^+, 100%), 591.20 (2M + Na^+, 20%). ^{1}H NMR (600 MHz, $CDCl_3$) δ/ppm: 7.75–7.69 (m, 2H), 7.38 (d, *J* = 5.0 Hz, 4H), 7.34–7.29 (m, 1H), 6.69–6.64 (m, 2H), 6.62 (d, *J* = 6.7 Hz, 1H), 5.25 (td, *J* = 6.3, 3.7 Hz, 1H), 4.07–3.91 (m, 2H), 3.02 (s, 6H). ^{13}C NMR (151 MHz, CD_3OD) δ/ppm: 170.34, 154.31, 141.78, 129.91, 129.43, 129.42, 128.26, 128.01, 128.01, 121.99, 112.11, 66.18, 57.48, 40.24.

$Phg^{\#}$–$C_{16}H_9$. 1-Pyrenecarboxylic acid (2.0 mmol, 492.52 mg), TBTU (2.0 mmol, 642.2 mg), HOBt (2.0 mmol, 306.2 mg), (*S*)-phenylglycinol ($Phg^{\#}$, 2.0 mmol, 274.4 mg), DIPEA (8.0 mmol, 1.394 mL). *Flash* chromatography, prepacked silicagel column, 3% CH_3OH in CH_2Cl_2. Yield: 477.7 mg (1.31 mmol, 65%), yellow solid. ^{1}H NMR (600 MHz, CD_3CN) δ/ppm: 8.50 (d, *J* = 9.2 Hz, 1H), 8.34–8.27 (m, 3H), 8.25–8.16 (m, 4H), 8.10 (t, *J* = 7.6 Hz, 1H), 7.55 (s, 1H), 7.53–7.48 (m, 2H), 7.43 (dd, *J* = 8.5, 6.9 Hz, 2H), 7.37–7.31 (m, 1H), 5.35 (td, *J* = 7.8, 5.0 Hz, 1H), 4.09–3.75 (m, 2H), 3.19 (t, *J* = 5.9 Hz, 1H). ^{13}C NMR (151 MHz, CD_3OD) δ/ppm: 141.44, 133.85, 132.77, 132.64, 132.15, 129.66, 129.64, 129.50, 128.60, 128.26, 128.21, 127.54, 126.91, 126.77, 126.04, 125.78, 125.57, 125.52, 125.47, 66.28, 58.08.

$Phg^{\#}$–*m*C_6H_4–$(AlaOMe)_2$. Trimesic acid (2.0 mmol, 420.28 mg), HATU (first-day addition: 3.0 mmol, 1140.71 mg; second-day addition: 3.1 mmol, 1178.7 mg), DIPEA (first-day addition: 10.0 mmol, 1.743 mL; second-day addition: 14.4 mmol, 2.509 mL), (*S*)-Ala–OMe·HCl (3.1 mmol, 405.2 mg), (*S*)-phenylglycinol (3.1 mmol, 425.3 mg). *Flash* chromatography, prepacked silicagel column, 2% → 10% CH_3OH in CH_2Cl_2. Yield: 181.8 mg (0.36 mmol, 23%), white solid. ^{1}H NMR (600 MHz, $CDCl_3$) δ/ppm: 8.09 (d, *J* = 1.6 Hz, 2H), 8.07 (t, *J* = 1.6 Hz, 1H), 7.74 (d, *J* = 7.6 Hz, 2H), 7.68 (d, *J* = 7.6 Hz, 1H), 7.45–7.40 (m, 2H), 7.38 (dd, *J* = 8.5, 6.9 Hz, 2H), 7.32–7.26 (m, 1H), 5.30 (td, *J* = 7.8, 3.2 Hz, 1H), 4.78 (p, *J* = 7.4 Hz, 2H), 3.99 (d, *J* = 34.5 Hz, 3H), 3.80 (s, 6H), 1.56 (d, *J* = 7.4 Hz, 6H). ^{13}C NMR (151 MHz, CD_3OD) δ/ppm: 168.53, 141.11, 136.88, 136.09, 130.48, 130.39, 129.57, 128.53, 128.09, 66.00, 58.02, 52.85, 50.27, 17.22.

Phg$^{\#,*}$–*m*C$_6$H$_4$–(AlaOMe)$_2$. Trimesic acid (2.0 mmol, 420.28 mg), HATU (first-day addition: 3.0 mmol, 1140.71 mg; second-day addition: 3.1 mmol, 1178.7 mg), DIPEA (first-day addition: 10.0 mmol, 1.743 mL; second-day addition: 14.4 mmol, 2.509 mL), (*S*)-Ala–OMe·HCl (3.1 mmol, 405.2 mg), (*R*)-phenylglycinol (3.1 mmol, 425.3 mg). *Flash* chromatography, prepacked silicagel column, 2% → 10% CH_3OH in CH_2Cl_2. Yield: 158.4 mg (0.32 mmol, 16%), white solid. ^{1}H NMR (600 MHz, $CDCl_3$) δ/ppm: 8.21 (d, J = 1.6 Hz, 2H), 8.15 (t, J = 1.7 Hz, 1H), 7.76 (d, J = 7.6 Hz, 2H), 7.54 (d, J = 7.7 Hz, 1H), 7.51–7.45 (m, 2H), 7.44–7.34 (m, 2H), 7.31–7.25 (m, 1H), 5.31 (td, J = 7.1, 4.1 Hz, 1H), 4.75 (quin., J = 7.4 Hz, 2H), 4.07–3.98 (m, 2H), 3.80–3.77 (m, 1H), 3.75 (s, 6H), 1.56 (d, J = 7.4 Hz, 6H). ^{13}C NMR (151 MHz, CD_3OD) δ/ppm: 173.27, 167.15, 139.71, 135.49, 134.71, 129.08, 129.00, 128.16, 127.12, 126.69, 100.00, 64.59, 56.63, 51.44, 48.87, 15.81.

General oxazoline synthesis procedure

Diethylaminosulfur trifluoride (1.5 equivalents) was added dropwise to a cooled solution (−78 °C) of precursor (1 equivalent) in dry CH_2Cl_2 (14 mL). After stirring for 1 h at −78 °C, anhydrous K_2CO_3 (1.5 equivalents) was added in one portion and the mixture was allowed to warm to room temperature. The reaction was quenched with saturated aqueous $NaHCO_3$ (20 mL). The biphasic mixture was extracted with EtOAc (3 × 40 mL). The combined organic extracts were washed with water (100 mL) and NaCl (sat. aq., 100 mL), dried over anhydrous Na_2SO_4 and evaporated under reduced pressure to yield the crude product.[51]

(Ph-ox)–C$_6$H$_5$ (1$_H$). Phg$^{\#}$–C$_6$H$_5$ (1.93 mmol, 465.7 mg). *Flash* chromatography, prepacked silicagel column, EtOAc : hexane = 2 : 8 → 3 : 7. Yield: 329.9 mg (1.5 mmol, 77%), colorless oil. M_r($C_{15}H_{13}NO$) = 223.10. ESI-MS (m/z): 224.10 (M + H$^+$, 100%). ^{1}H NMR (600 MHz, $CDCl_3$) δ/ppm: 8.08–8.01 (m, 2H), 7.55–7.27 (m, 8H), 5.39 (dd, J = 10.1, 8.1 Hz, 1H), 4.80 (dd, J = 10.1, 8.4 Hz, 1H), 4.28 (t, J = 8.3 Hz, 1H). ^{1}H NMR (300 MHz, CD_3CN) δ/ppm: 8.08–7.93 (m, 2H), 7.60–7.44 (m, 3H), 7.42–7.24 (m, 4H), 5.38 (dd, J = 10.1, 8.1 Hz, 1H), 4.82 (dd, J = 10.1, 8.5 Hz, 1H), 4.22 (t, J = 8.3 Hz, 1H). ^{13}C NMR (151 MHz, $CDCl_3$) δ/ppm: 164.88, 142.53, 131.68, 128.89, 128.61, 128.52, 127.76, 127.71, 126.89, 75.02, 70.27. MALDI-HRMS (m/z): expected 224.11 (M + H$^+$), 246.09 (M + Na$^+$); observed 224.1068, 246.0887. IR (ATR): 3063 (w), 3032 (w), 2967 (w), 2898 (w), 1646 (s), 1495 (m), 1450 (m), 1357 (m), 1066 (m), 1025 (m), 950 (m), 789 (m), 691 (s), 678 (s). UV–vis [CH_2Cl_2, c (1$_H$) = 0.03 mM; λ_{max}, nm (ε_{UV}, M^{-1} cm^{-1})]: 247 (12 333). UV–vis [CH_2Cl_2, c (1$_H$) = 0.15 mM; λ_{max}, nm (ε_{UV}, M^{-1} cm^{-1})]: 247 (10 884). CD [CH_2Cl_2, c (1$_H$) = 0.03 mM; θ_{max}, nm (ε_{CD}, M^{-1} cm^{-1})]: 249 (−3.94), 257 (−3.78), 283 (0.62). CD [CH_2Cl_2, c (1$_H$) = 0.15 mM; θ_{max}, nm (ε_{CD}, M^{-1} cm^{-1})]: 283 (0.67), 290 (11).

(Ph-ox)–*p*C$_6$H$_4$–F (1$_F$). Phg$^{\#}$–*p*C$_6$H$_4$F (1.93 mmol, 509.1 mg). *Flash* chromatography, prepacked silicagel column, EtOAc : hexane = 2 : 8 → 3 : 7. Yield: 324.6 mg (1.35 mmol, 70%), white solid. M_r($C_{15}H_{12}FNO$) = 241.10. ESI-MS (m/z): 242.15 (M + H$^+$, 100%). ^{1}H NMR (600 MHz, $CDCl_3$) δ/ppm: 8.11–7.97 (m, 2H), 7.41–7.27 (m, 5H), 7.12 (t, J = 8.7 Hz, 2H), 5.38 (dd, J = 10.1, 8.2 Hz, 1H), 4.80 (dd, J = 10.1, 8.3 Hz, 1H), 4.28 (t, J = 8.3 Hz, 1H). ^{13}C NMR (151 MHz, $CDCl_3$) δ/ppm: 165.83, 164.16, 163.96, 142.40, 130.91, 130.86, 128.93, 127.83, 126.87, 123.99, 123.97, 115.74, 115.59, 75.15, 70.32. ^{1}MALDI-HRMS (m/z): expected 242.10 (M + H$^+$); observed 242.0971. IR (ATR): 3071 (w), 3034 (w), 2971 (w), 2907 (w), 1646 (s), 1601 (m), 1506 (s), 1497 (m), 1474 (m), 1457 (m), 1411 (m), 1364 (m), 1349 (m), 1316 (m), 1219 (m), 1146 (m), 1071 (s), 952 (s), 846 (s), 813 (m), 759 (s), 736 (m), 697 (s), 671 (s). UV–vis [CH_2Cl_2, c (1$_F$) = 0.03 mM; λ_{max}, nm (ε_{UV}, M^{-1} cm^{-1})]: 246 (12 697). UV–vis [CH_2Cl_2, c (1$_F$) = 0.15 mM; λ_{max}, nm (ε_{UV}, M^{-1} cm^{-1})]: 246 (10 929). CD [CH_2Cl_2, c (1$_F$) = 0.03 mM; θ_{max}, nm (ε_{CD}, M^{-1} cm^{-1})]: 249 (−3.69), 257 (−3.65).

(Ph-ox)–*p*C$_6$H$_4$–NMe$_2$ (1$_N$). Phg$^{\#}$–*p*C$_6$H$_4$–NMe$_2$ (1.75 mmol, 497.7 mg). *Flash* chromatography, prepacked silicagel column, EtOAc : hexane = 2 : 8 → 3 : 7. Yield: 331.7 mg (1.25 mmol, 71%), white solid. M_r($C_{17}H_{18}N_2O$) = 266.12. ESI-MS (m/z): 267.15 (M + H$^+$, 100%). ^{1}H NMR (300 MHz, $CDCl_3$) δ/ppm: 8.01–7.71 (m, 2H), 7.52–7.10 (m, 5H), 6.85–6.43 (m, 2H), 5.33 (dd, J = 9.9, 7.8 Hz, 1H), 4.73 (dd, J = 10.0, 8.3 Hz, 1H), 4.21 (t, J = 8.1 Hz, 1H), 3.03 (s, 6H). ^{13}C NMR (151 MHz, $CDCl_3$) δ/ppm: 165.29, 152.58, 143.22, 129.96, 128.78, 127.53, 126.93, 114.79, 111.27, 74.71, 70.13, 40.26. MALDI-HRMS (m/z): expected 267.15 (M + H$^+$); observed 267.1813. IR (ATR): 2989 (w), 2892 (w), 2822 (w), 1634 (m), 1605 (m), 1523 (m), 1359 (m), 1182 (m), 1075 (m), 975 (m), 950 (m), 818 (m), 755 (m), 742 (m), 699 (m), 669 (m). UV–vis [CH_2Cl_2, c (1$_N$) = 0.03 mM; λ_{max}, nm (ε_{UV}, M^{-1} cm^{-1})]: 232 (7725), 309 (28 743). UV–vis [CH_2Cl_2, c (1$_N$) = 0.15 mM; λ_{max}, nm (ε_{UV}, M^{-1} cm^{-1})]: 233 (13 223). CD [CH_2Cl_2, c (1$_N$) = 0.03 mM; θ_{max}, nm (ε_{CD}, M^{-1} cm^{-1})]: 256 (−0.31), 262 (0.69), 269 (0.95), 318 (−0.93).

(Ph-ox)–C$_{16}$H$_9$ (1$_P$). Phg$^{\#}$–C$_{16}$H$_9$ (1.22 mmol, 450.0 mg). *Flash* chromatography, prepacked silicagel column, EtOAc : hexane = 2 : 8 → 3 : 7. Yield: 293.5 mg (0.84 mmol, 71%), white solid. ^{1}H NMR (600 MHz, $CDCl_3$) δ/ppm: 9.55 (d, J = 9.4 Hz, 1H), 8.66 (d, J = 8.0 Hz, 1H), 8.26 (ddd, J = 7.4, 5.9, 1.1 Hz, 2H), 8.22 (d, J = 8.7 Hz, 2H), 8.19–8.09 (m, 2H), 8.06 (t, J = 7.6 Hz, 1H), 7.50–7.45 (m, 2H), 7.42 (dd, J = 8.5, 6.9 Hz, 2H), 7.37–7.31 (m, 1H), 5.66 (dd, J = 10.2, 8.3 Hz, 1H), 4.94 (dd, J = 10.2, 8.1 Hz, 1H), 4.40 (t, J = 8.2 Hz, 1H). ^{13}C NMR (151 MHz, $CDCl_3$) δ/ppm: 165.44, 142.82, 133.62, 131.27, 130.72, 130.64, 129.24, 129.17, 128.98, 128.07, 127.79, 127.39, 126.99, 126.34, 126.11, 126.06, 125.84, 125.01, 124.47, 124.40, 121.22, 74.22, 71.23. M_r($C_{25}H_{17}NO$) = 347.13. ESI-MS (m/z): 348.10 (M + H$^+$, 100%), 695.1 (2M + H$^+$). MALDI-HRMS (m/z): expected 348.14 (M + H$^+$); observed 348.1556. IR (ATR): 3055 (w). 2924 (w), 1659 (w), 1646 (w), 1623 (w), 1610 (w), 1606 (w), 1588 (w), 1567 (w), 1536 (w), 1517 (w), 1463 (w), 1413 (w), 1359 (w), 1295 (w), 1275 (w), 1264 (w), 1219 (w), 1155 (w), 1107 (w), 1047 (m), 868 (m), 779 (m), 721 (m). UV–vis [CH_2Cl_2, c (1$_P$) = 0.03 mM; λ_{max}, nm (ε_{UV}, M^{-1} cm^{-1})]: 242 (51 808), 274 (sh, 31 382), 352 (37 033), 384 (11 025). CD [CH_2Cl_2, c (1$_P$) = 0.03 mM; θ_{max}, nm (ε_{CD}, M^{-1} cm^{-1})]: 248 (0.67), 259 (−0.08), 285 (−0.62), 333 (0.25), 339 (0.25), 370 (0.25), 384 (0.18).

(Ph-ox)–*m*C$_6$H$_4$–(AlaOMe)$_2$ (1$_{m2A}$). Phg$^{\#}$–*m*C$_6$H$_4$–(AlaOMe)$_2$ (0.30 mmol, 149.86 mg). *Flash* chromatography, prepacked sili-

cagel column, EtOAc : hexane = 1 : 1 → pure EtOAc. Yield: 138.6 mg (0.29 mmol, 96%), white solid. ^{1}H NMR (600 MHz, $CDCl_3$) δ/ppm: 8.54 (d, J = 1.7 Hz, 2H), 8.41 (t, J = 1.7 Hz, 1H), 7.40–7.29 (m, 5H), 6.99 (d, J = 7.4 Hz, 2H), 5.42 (dd, J = 10.1, 8.4 Hz, 1H), 4.87 (dd, J = 10.2, 8.4 Hz, 1H), 4.82 (p, J = 7.2 Hz, 2H), 4.35 (t, J = 8.4 Hz, 1H), 3.79 (s, 6H), 1.52 (d, J = 7.2 Hz, 6H). ^{13}C NMR (151 MHz, $CDCl_3$) δ/ppm: 173.74, 165.59, 163.83, 141.81, 134.80, 129.81, 129.06, 129.03, 128.51, 128.06, 127.15, 75.50, 70.58, 60.52, 52.70, 48.86, 17.97. $M_r(C_{25}H_{27}N_3O_7)$ = 481.18. ESI-MS (m/z): 482.20 (M + H$^+$, 87%), 963.3 (2M + H$^+$, 100%). MALDI-HRMS (m/z): expected 482.19 (M + H$^+$); observed 482.2140. IR (ATR): 3271 (w), 3068 (w), 3032 (w), 2989 (w), 2954 (w), 2905 (w), 2851 (w), 2085 (w), 1741 (m), 1649 (m), 1595 (w), 1530 (m), 1450 (m), 1439 (m), 1377 (w), 1357 (w), 1338 (w), 1319 (w), 1269 (m), 1207 (m), 1159 (m), 1099 (m), 1049 (m), 982 (sh m), 967 (m), 021 (m), 906 (w), 876 (w), 841 (w), 762 (w), 701 (m). UV–vis [CH_2Cl_2, c ($\mathbf{1_{m2A}}$) = 0.03 mM; λ_{max}, nm (ε_{UV}, M^{-1} cm^{-1})]: 256 (sh, 13 445). CD [CH_2Cl_2, c ($\mathbf{1_{m2A}}$) = 0.03 mM; θ_{max}, nm (ε_{CD}, M^{-1} cm^{-1})]: 237 (−3.90), 252 (2.04), 280 (−1.01).

((*R*)-Ph-ox)–*m*C$_6$H$_4$–(AlaOMe)$_2$ ($\mathbf{1_{m2A}}$*). Phg$^{\#,*}$–*m*C$_6$H$_4$–(AlaOMe)$_2$ (0.44 mmol, 220.00 mg). *Flash* chromatography, pre-packed silicagel column, EtOAc : hexane = 1 : 1 → pure EtOAc. Yield: 182.5 mg (0.38 mmol, 87%), white solid. ^{1}H NMR (600 MHz, $CDCl_3$) δ/ppm: 8.47 (d, J = 1.7 Hz, 2H), 8.37 (t, J = 1.7 Hz, 1H), 7.42–7.34 (m, 4H), 7.31 (ddd, J = 6.5, 3.5, 2.0 Hz, 3H), 5.42 (dd, J = 10.2, 8.2 Hz, 1H), 4.86–4.76 (m, 3H), 4.31 (t, J = 8.3 Hz, 1H), 3.77 (s, 3H), 1.49 (d, J = 7.3 Hz, 3H). ^{13}C NMR (151 MHz, $CDCl_3$) δ/ppm: 173.87, 165.74, 163.94, 141.83, 134.73, 129.79, 129.29, 129.01, 128.24, 128.04, 127.00, 75.42, 70.19, 52.70, 48.82, 48.80, 17.84. $M_r(C_{25}H_{27}N_3O_7)$ = 481.18. ESI-MS (m/z): 482.20 (M + H$^+$, 93%), 963.95 (2M + H$^+$, 100%). MALDI-HRMS (m/z): expected 482.19 (M + H$^+$); observed 482.2108. IR (ATR): 3371 (sh w), 3278 (w), 3064 (w), 2987 (w), 2952 (w), 2093(w), 1736 (m), 1649 (s), 1597 (m), 1528 (m), 1450 (m), 1379 (sh w), 1346 (sh m), 1275 (m), 1210 (s), 1159 (m), 1098 (m), 1051 (m), 980 (m), 924 (m), 848 (w), 759 (m), 701 (s). UV–vis [CH_2Cl_2, c ($\mathbf{1_{m2A}}$*) = 0.030 mM; λ_{max}, nm (ε_{UV}, M^{-1} cm^{-1})] 256 (sh, 12 749). CD [CH_2Cl_2, c ($\mathbf{1_{m2A}}$*) = 0.030 mM; θ_{max}, nm (ε_{CD}, M^{-1} cm^{-1})]: 239 (12.77), 262 (4.25), 271 (3.14).

Metal complex synthesis

All transition metal complexes were prepared *in situ* in CH_2Cl_2. The metal precursor was weighed in a glass vial and dissolved in 2.5 mL CH_2Cl_2 or CH_2Cl_2 and CH_3CN or CH_3OH (2 : 1) solution (cadmium and non-halide precursors). The ligand solution in CH_2Cl_2 was added (2.5 mL) and everything stirred for 4 h. The solutions were filtered over blue ribbon filter paper, and the solvent evaporated under reduced pressure. The solids were washed three times with non-polar solvent mixture to remove excess ligand (8 : 2 = hexane : EtOAc for $\mathbf{1_H}$ and $\mathbf{1_F}$, 1 : 1 = hexane : EtOAc for all other ligands) dried, re-dissolved in CH_2Cl_2/CH_3CN. Without further purification, hexane (5 mL) was layered over the complex solutions and left partially closed for slow evaporation, yielding single crystals as needles or rhombs over the course of few days. Portions of single crystals were isolated for NMR, SC XRD and PD XRD analysis.

[Zn($\mathbf{1_H}$)$_2$Br$_2$]. (Ph-ox)–C$_6$H$_5$ ($\mathbf{1_H}$) (0.10 mmol, 22.3 mg), $ZnBr_2$ (0.049 mmol, 11.0 mg). Rhomb-like colorless single crystals were obtained after 2 days. Yield: 26.7 mg (0.04 mmol, 82%). $M_r(C_{30}H_{26}Br_2N_2O_2Zn)$ = 667.97. ^{1}H NMR (600 MHz, $CDCl_3$) δ/ppm: 8.06 (dt, J = 7.1, 1.3 Hz, 2H), 7.68 (t, J = 7.5 Hz, 1H), 7.54–7.49 (m, 2H), 7.36–7.32 (m, 4H), 7.31–7.27 (m, 1H), 5.87 (t, J = 7.3 Hz, 1H), 4.40 (dd, J = 8.6, 4.8 Hz, 1H), 4.24 (s, 1H). ^{1}H NMR (300 MHz, CD_3CN) δ/ppm: 8.06–8.00 (m, 1H), 7.67–7.61 (m, 1H), 7.57–7.26 (m, 7H), 5.55 (s, 1H), 4.90–4.53 (m, 1H), 4.30 (dd, J = 8.7, 6.9 Hz, 1H). ^{13}C NMR (151 MHz, $CDCl_3$) δ/ppm: 139.46, 133.88, 130.74, 129.11, 128.63, 128.47, 127.06, 124.83, 76.19, 68.10. IR (ATR): 3062 (w), 2372 (w), 2346 (w), 1720 (w), 1703 (w), 1616 (m), 1601 (m), 1573 (m), 1497 (w), 1474 (w), 1451 (m), 1385 (m), 1275 (w), 1237 (m), 1120 (m), 943 (m), 759 (m), 695 (s). UV–vis [CH_2Cl_2, c ([Zn($\mathbf{1_H}$)$_2$Br$_2$]) = 0.015 mM; λ_{max}, nm (ε_{UV}, M^{-1} cm^{-1})]: 241 (19 289). UV–vis [CH_2Cl_2, c ([Zn($\mathbf{1_H}$)$_2$Br$_2$]) = 0.075 mM; λ_{max}, nm (ε_{UV}, M^{-1} cm^{-1})]: 241 (18 639). CD [CH_2Cl_2, c ([Zn($\mathbf{1_H}$)$_2$Br$_2$]) = 0.015 mM; θ_{max}, nm (ε_{CD}, M^{-1} cm^{-1})]: 250 (−5.10), 257 (−4.83), 282 (0.73), 287 (0.41). CD [CH_2Cl_2, c ([Zn($\mathbf{1_H}$)$_2$Br$_2$]) = 0.075 mM; θ_{max}, nm (ε_{CD}, M^{-1} cm^{-1})]: 283 (1.12), 290 (sh, 0.77).

[Zn($\mathbf{1_F}$)$_2$Br$_2$]·CH$_3$CN. (Ph-ox)–C$_6$H$_4$F ($\mathbf{1_F}$) (0.10 mmol, 24.1 mg), $ZnBr_2$ (0.049 mmol, 11.0 mg). Rod-like colorless single crystals were obtained after 2 days. Single crystals turn to white powder after solvent is evaporated. Yield: 24.7 mg (0.035 mmol, 71%). ^{1}H NMR (600 MHz, $CDCl_3$) δ/ppm: 8.09 (dd, J = 8.7, 5.3 Hz, 2H), 7.39–7.29 (m, 5H), 7.17 (t, J = 8.5 Hz, 2H), 5.84 (s, 1H), 4.67–4.28 (m, 2H). ^{13}C NMR (151 MHz, $CDCl_3$) δ/ppm: 166.83, 165.11, 129.16, 129.15, 128.68, 127.08, 115.91, 115.76, 76.16, 68.59. IR (ATR): 3067 (w), 2367 (w), 2346 (w), 1616 (m), 1604 (s), 1509 (s), 1470 (m), 1416 (m), 1377 (m), 1305 (m), 1236 (s), 1266 (s), 1161 (s), 1100 (m), 945 (s), 928 (m), 851 (s), 813 (m), 759 (s), 749 (s), 732 (s), 699 (s), 690 (s). UV–vis [CH_2Cl_2, c ([Zn($\mathbf{1_F}$)$_2$Br$_2$]) = 0.015 mM; λ_{max}, nm (ε_{UV}, M^{-1} cm^{-1})]: 245 (24 467). UV–vis [CH_2Cl_2, c ([Zn($\mathbf{1_F}$)$_2$Br$_2$]) = 0.075 mM; λ_{max}, nm (ε_{UV}, M^{-1} cm^{-1})]: 246 (21 702). CD [CH_2Cl_2, c ([Zn($\mathbf{1_F}$)$_2$Br$_2$]) = 0.015 mM; θ_{max}, nm (ε_{CD}, M^{-1} cm^{-1})]: 249 (−5.78), 257 (−5.58).

[Zn($\mathbf{1_N}$)$_2$Br$_2$]·CH$_2$Cl$_2$. (Ph-ox)–C$_6$H$_4$NMe$_2$ ($\mathbf{1_N}$)(0.10 mmol, 26.6 mg), $ZnBr_2$ (0.049 mmol, 11.0 mg). Rod-like colorless single crystals were obtained after 2 days. Single crystals turn to white powder after solvent is evaporated. Yield: 29.1 mg (0.038 mmol, 78%). ^{1}H NMR (600 MHz, $CDCl_3$) δ/ppm: 7.97 (d, J = 8.5 Hz, 2H), 7.39–7.28 (m, 4H), 7.26–7.21 (m, 1H), 6.69 (d, J = 8.9 Hz, 2H), 5.93 (s, 1H), 4.31 (s, 1H), 4.07 (s, 1H), 3.09 (s, 6H). ^{13}C NMR (151 MHz, $CDCl_3$) δ/ppm: 152.62, 131.49, 130.59, 127.79, 126.98, 125.72, 109.75, 109.28, 74.38, 66.18, 39.15. IR (ATR): 2900 (w), 2367 (w), 2346 (w), 1608 (sh), 1590 (s), 1579 (s), 1521 (s), 1439 (m), 1374 (s), 1236 (m), 1196 (s), 1172 (m), 1109 (m), 943 (m), 924 (m), 820 (m), 749 (m), 736 (m), 693 (s). UV–vis [CH_2Cl_2, c ([Zn($\mathbf{1_N}$)$_2$Br$_2$]) = 0.015 mM; λ_{max}, nm (ε_{UV}, M^{-1} cm^{-1})]: 233 (14 704), 319 (42 821), 338 (sh, 35 199), 373 (5105). UV–vis [CH_2Cl_2, c ([Zn($\mathbf{1_N}$)$_2$Br$_2$]) = 0.075 mM; λ_{max}, nm (ε_{UV}, M^{-1} cm^{-1})]: 234 (15 629). CD

$[CH_2Cl_2$, c ($[Zn(\mathbf{1_N})_2Br_2]$) = 0.015 mM; θ_{max}, nm (ε_{CD}, M^{-1} cm^{-1})]: 246 (7.30), 268 (−1.19), 318 (9.26), 347 (−10.48). CD $[CH_2Cl_2$, c ($[Zn(\mathbf{1_N})_2Br_2]$) = 0.075 mM; θ_{max}, nm (ε_{CD}, M^{-1} cm^{-1})]: 356 (−4.59).

$[Zn(\mathbf{1_P})_2Br_2]$. (Ph-ox)–$C_{16}H_9$ ($\mathbf{1_P}$) (0.10 mmol, 34.9 mg), $ZnBr_2$ (0.049 mmol, 11.0 mg). Yield: 22.9 mg (0.025 mmol, 51%), yellow solid. ^{1}H NMR (600 MHz, $CDCl_3$) δ/ppm: 9.16 (s, 1H), 8.21 (d, J = 7.5 Hz, 1H), 8.13 (dd, J = 14.7, 8.4 Hz, 2H), 7.99 (d, J = 8.7 Hz, 1H), 7.91 (t, J = 7.6 Hz, 1H), 7.47 (d, J = 7.5 Hz, 2H), 7.39 (t, J = 7.5 Hz, 2H), 7.33 (t, J = 7.3 Hz, 1H), 7.11–6.31 (m, 3H), 6.13 (s, 1H), 4.74 (s, 1H), 4.58 (t, J = 6.6 Hz, 1H). ^{13}C NMR (151 MHz, $CDCl_3$) δ/ppm: 130.83, 130.38, 129.35, 129.21, 129.05, 127.58, 127.09, 126.76, 126.68, 126.63, 124.26, 123.72, 119.18, 108.69, 31.73, 22.80, 14.26. IR (ATR): 3073 (w), 2928 (w), 1620(w), 1603 (w), 1588 (w), 1567 (w), 1536 (w), 1517 (w), 1498 (w), 1483 (w), 1478 (w), 1446 (w), 1401 (w), 1325 (w), 1310 (w), 1269 (w), 1262 (w), 1234 (w), 1210 (w), 1157 (w), 1116 (w), 1072 (w), 1025 (w), 970 (w), 882 (w), 885 (w), 775 (m), 729 (m). UV–vis $[CH_2Cl_2$, c ($[Zn(\mathbf{1_P})_2Br_2]$) = 0.015 mM; λ_{max}, nm (ε_{UV}, M^{-1} cm^{-1})]: 233 (14 704), 319 (42 821), 338 (sh, 35 199), 373 (5105). UV–vis $[CH_2Cl_2$, c ($[Zn(\mathbf{1_P})_2Br_2]$) = 0.075 mM; λ_{max}, nm (ε_{UV}, M^{-1} cm^{-1})]: 234 (15 629). CD $[CH_2Cl_2$, c ($[Zn(\mathbf{1_P})_2Br_2]$) = 0.015 mM; θ_{max}, nm (ε_{CD}, M^{-1} cm^{-1})]: 246 (7.30), 268 (−1.19), 318 (9.26), 347 (−10.48). CD $[CH_2Cl_2$, c ($[Zn(\mathbf{1_P})_2Br_2]$) = 0.075 mM; θ_{max}, nm (ε_{CD}, M^{-1} cm^{-1})]: 356 (−4.59).

$[Zn(\mathbf{1_{mA}})_2Br_2]$. (Ph-ox)–$m$$C_6H_4$–AlaOMe ($\mathbf{1_{mA}}$)(0.10 mmol, 35.2 mg), $ZnBr_2$ (0.049 mmol, 11.0 mg). Thin rod-like colorless single crystals were obtained after 1 day. Yield: 31.9 mg (0.034 mmol, 69%). ^{1}H NMR (600 MHz, $CDCl_3$) δ/ppm: 9.23 (s, 1H), 8.53 (d, J = 7.9 Hz, 1H), 8.14 (d, J = 6.4 Hz, 1H), 7.59 (t, J = 7.8 Hz, 1H), 7.43–7.28 (m, 7H), 6.24 (dd, J = 9.7, 4.3 Hz, 1H), 4.77–4.69 (m, 1H), 4.53 (dd, J = 9.2, 4.4 Hz, 1H), 4.46–4.39 (m, 1H), 3.78 (s, 3H), 1.73 (d, J = 7.4 Hz, 3H). ^{13}C NMR (151 MHz, $CDCl_3$) δ/ppm: 174.76, 165.29, 164.45, 139.32, 135.06, 133.61, 132.69, 129.43, 129.03, 128.65, 127.72, 127.21, 77.50, 68.13, 52.58, 49.83, 29.84, 17.25. IR (ATR): 3412 (w), 3382 (w), 2984 (w), 1776 (m), 1759 (m), 1698 (m), 1692 (m), 1638 (w), 1599 (w), 1547 (m), 1483 (w), 1463 (w), 1398 (w), 1381 (w), 1329 (w), 1256 (m), 1198 (w), 1165 (m), 1107 (w), 1081 (w), 1010 (w), 984 (w), 967 (w), 846 (w), 781 (m), 740 (m), 727 (m). UV–vis $[CH_2Cl_2$, c ($[Zn(\mathbf{1_{mA}})_2Br_2]$) = 0.015 mM; λ_{max}, nm (ε_{UV}, M^{-1} cm^{-1})] 255 (sh, 18 663). CD $[CH_2Cl_2$, c ($[Zn(\mathbf{1_{mA}})_2Br_2]$) = 0.015 mM; θ_{max}, nm (ε_{CD}, M^{-1} cm^{-1})]: 236 (13.22), 290 (2.24).

$[Zn(\mathbf{1_{mA}}^*)_2Br_2]$. ((*R*)-Ph-ox)–$m$$C_6H_4$–AlaOMe ($\mathbf{1_{mA}}^*$) (0.07 mmol, 24.65 mg), $ZnBr_2$ (0.035 mmol, 7.82 mg). Yield: 15.65 mg (0.017 mmol, 48%), white solid. ^{1}H NMR (600 MHz, $CDCl_3$) δ/ppm: 8.84 (s, 1H), 8.22 (s, 1H), 7.85 (d, J = 7.6 Hz, 2H), 7.59 (t, J = 7.8 Hz, 1H), 7.42–7.29 (m, 5H), 5.87 (t, J = 6.8 Hz, 1H), 4.71 (quin., J = 7.2 Hz, 2H), 4.56 (s, 1H), 3.74 (s, 3H), 1.56 (s, 3H). ^{13}C NMR (151 MHz, $CDCl_3$) δ/ppm: 173.29, 166.35, 166.11, 134.31, 133.75, 133.22, 129.58, 129.32, 128.98, 127.15, 76.76, 67.59, 52.95, 49.27, 16.85. IR (ATR): 3330 (w), 3056 (w), 2954 (w), 2851 (w), 2107 (w), 1736 (m), 1638 (m), 1625 (m), 1579 (m), 1528 (m), 1493 (m), 1454 (m), 1377 (m), 1349 (m), 1302 (m), 1237 (sh m), 1211 (m), 1169 (m), 1135 (m), 1081 (m), 1049 (m), 984 (m), 962 (m), 937 (m), 883 (w), 846 (w), 822 (w), 757 (sh m), 731 (m), 714 (m), 697 (m). UV–vis $[CH_2Cl_2$, c ($[Zn(\mathbf{1_{mA}}^*)_2Br_2]$) = 0.015 mM; λ_{max}, nm (ε_{UV}, M^{-1} cm^{-1})]: 254 (sh, 19 049). CD $[CH_2Cl_2$, c ($[Zn(\mathbf{1_{mA}}^*)_2Br_2]$) = 0.015 mM; θ_{max}, nm (ε_{CD}, M^{-1} cm^{-1})]: 250 (6.38), 292 (−0.95).

$[Zn(\mathbf{1_{m2A}})_2Br_2]$. (Ph-ox)–$m$$C_6H_4$–(AlaOMe)$_2$ ($\mathbf{1_{m2A}}$)(0.10 mmol, 48.2 mg), $ZnBr_2$ (0.049 mmol, 11.0 mg). Thin plate-like colorless single crystals were obtained after storing at −5 °C for 2 days. Yield: 33.2 mg (0.027 mmol, 56%). ^{1}H NMR (600 MHz, $CDCl_3$) δ/ppm: 8.94 (s, 1H), 8.77–8.40 (s, 2H), 8.21–7.89 (s, 2H), 7.58–7.30 (m, 5H), 6.11 (s, 1H), 4.81 (p, J = 7.2 Hz, 2H), 4.51 (dd, J = 9.1, 4.7 Hz, 1H), 4.27 (s, 1H), 3.80 (s, 6H), 1.65 (d, J = 7.3 Hz, 6H). ^{13}C NMR (151 MHz, CD_3CN) δ/ppm: 173.91, 166.00, 165.28, 135.32, 131.75, 129.60, 128.10, 67.36, 55.69, 52.63, 49.67, 17.20. IR (ATR): 3356 (w), 3319 (w), 2948 (w), 2363 (w), 1744 (m), 1672 (m), 1638 (m), 1543 (m), 1519 (m), 1450 (w), 1388 (w), 1347 (w), 1303 (w), 1265 (w), 1211 (m), 1163 (m), 1057 (w), 980 (w), 939 (w), 762 (w), 697 (m). UV–vis $[CH_2Cl_2$, c ($[Zn(\mathbf{1_{m2A}})_2Br_2]$) = 0.015 mM; λ_{max}, nm (ε_{UV}, M^{-1} cm^{-1})]: 254 (sh, 24 896). CD $[CH_2Cl_2$, c ($[Zn(\mathbf{1_{m2A}})_2Br_2]$) = 0.03 mM; θ_{max}, nm (ε_{CD}, M^{-1} cm^{-1})]: 258 (−13.87), 292 (2.05).

$[Zn(\mathbf{1_{m2A}}^*)_2Br_2]$. ((*R*)-Ph-ox)–$m$$C_6H_4$–(AlaOMe)$_2$ ($\mathbf{1_{m2A}}^*$) (0.07 mmol, 33.71 mg), $ZnBr_2$ (0.04 mmol, 7.82 mg). Yield: 27.50 mg (0.023 mmol, 66%). ^{1}H NMR (600 MHz, $CDCl_3$) δ/ppm: 8.57 (s, 2H), 7.90 (s, 1H), 7.44–7.29 (m, 5H), 5.73 (s, 1H), 4.77 (s, 2H), 4.47 (s, 1H), 3.77 (s, 6H), 1.60 (d, J = 7.3 Hz, 6H). ^{13}C NMR (151 MHz, CD_3CN) δ/ppm: 166.32, 134.61, 129.16, 128.82, 127.05, 68.52, 60.40, 52.66, 49.25, 17.59. IR (ATR): 3371 (sh w), 3065 (w), 2987 (w), 2952 (w), 2093(w), 1733 (m), 1647 (s), 1593 (m), 1528 (m), 1450 (m), 1381 (w), 1342 (sh m), 1303 (w), 1246 (sh m), 1215 (m), 1159 (m), 1126 (m), 1052 (m), 982 (m), 937 (w), 849 (w), 734 (m), 697 (m). UV–vis $[CH_2Cl_2$, c ($[Zn(\mathbf{1_{m2A}}^*)_2Br_2]$) = 0.015 mM; λ_{max}, nm (ε_{UV}, M^{-1} cm^{-1})] no maxima are present in CH_2Cl_2 in 233–800 nm range of wavelengths. CD $[CH_2Cl_2$, c ($[Zn(\mathbf{1_{m2A}}^*)_2Br_2]$) = 0.015 mM; θ_{max}, nm (ε_{CD}, M^{-1} cm^{-1})]: 237 (17.32), 252 (2.53), 261 (−2.39).

$[Zn(\mathbf{1_H})_2I_2]$. (Ph-ox)–C_6H_5 ($\mathbf{1_H}$)(0.15 mmol, 33.5 mg), ZnI_2 (0.075 mmol, 23.9 mg). Thin needle-like colorless single crystals were obtained after 2 days. Yield: 49.5 mg (0.065 mmol, 86%). ^{1}H NMR (600 MHz, $CDCl_3$) δ/ppm: 8.08 (d, J = 7.7 Hz, 2H), 7.67 (t, J = 7.5 Hz, 1H), 7.50 (t, J = 7.8 Hz, 2H), 7.39–7.29 (m, 5H), 6.00 (s, 1H), 4.66–4.17 (m, 2H). ^{13}C NMR (151 MHz, $CDCl_3$) δ/ppm: 166.25, 133.93, 133.66, 131.05, 130.06, 129.13, 128.79, 128.69, 128.43, 127.44, 124.75, 76.22, 68.74. IR (ATR): 1965 (w), 2366 (w), 2346 (w), 1614 (m), 1597 (m), 1571 (m), 1495 (m), 1472 (m), 1452 (m), 1381 (m), 1237 (m), 1120 (m), 1077 (m), 1027 (m), 943 (m), 803 (m), 759 (m), 695 (s). UV–vis $[CH_2Cl_2$, c ($[Zn(\mathbf{1_H})_2I_2]$.) = 0.075 mM; λ_{max}, nm (ε_{UV}, M^{-1} cm^{-1})]: 240 (21 237). CD $[CH_2Cl_2$, c ($[Zn(\mathbf{1_H})_2I_2]$) = 0.075 mM; θ_{max}, nm (ε_{CD}, M^{-1} cm^{-1})]: 287 (1.52).

$[Zn(\mathbf{1_H})_2(NO_3)_2]\cdot CH_2Cl_2$. (Ph-ox)–$C_6H_5$ ($\mathbf{1_H}$)(0.10 mmol, 22.3 mg), $Zn(NO_3)_2\cdot 4H_2O$ (0.049 mmol, 12.8 mg). Yield: 31.24 mg (0.044 mmol, 89%), white fibrous-cotton-like solid. ^{1}H NMR (600 MHz, CD_3OD) δ/ppm: 8.11–8.07 (m, 2H), 7.68–7.61 (m, 1H), 7.58–7.45 (m, 7H), 4.80 (dd, J = 7.8, 4.7 Hz, 1H), 4.72–4.61 (m, 2H). ^{13}C NMR (151 MHz, CD_3OD) δ/ppm: 167.33, 135.14, 134.73, 130.85, 130.81, 130.49, 129.67, 128.40,

66.40, 64.37, 55.33. IR (ATR): 3325 (b sh), 2907 (b), 2363 (w), 2344 (w), 1715 (s), 1602 (w), 1543 (m), 1390 (s), 1319 (s), 1256 (s), 1251 (sh), 1211 (m), 1180 (m), 1096 (m), 1070 (m), 1027 (m), 997 (m), 971 (m), 820 (m), 751 (m), 710 (s), 695 (s). UV–vis [CH_3CN; λ_{max}, nm (ε, M^{-1} cm^{-1})]: 194 (95 693), 227 (26 369), 274 sh (2780). CD [CH_3CN; θ_{max}, nm (ε_{CD}, M^{-1} cm^{-1})]: 205 (−2.56), 226 (1.23), 259 (−0.56).

[Cd($\mathbf{1_H}$)$_2$Br$_2$]. (Ph-ox)–C_6H_5 ($\mathbf{1_H}$)(0.20 mmol, 44.7 mg), $CdBr_2$ (0.099 mmol, 27.2 mg). Thin needle-like colorless single crystals were obtained after 2 days. Yield: 47.32 mg (0.065 mmol, 66%). ^{1}H NMR (600 MHz, CD_3CN) δ/ppm: 8.01 (dd, J = 8.3, 1.3 Hz, 2H), 7.60 (ddt, J = 8.8, 7.0, 1.3 Hz, 1H), 7.55–7.46 (m, 2H), 7.41–7.27 (m, 5H), 5.45 (dd, J = 10.1, 7.7 Hz, 1H), 4.82 (dd, J = 10.1, 8.6 Hz, 1H), 4.27 (dd, J = 8.6, 7.7 Hz, 1H). ^{13}C NMR (151 MHz, CD_3CN) δ/ppm: 142.65, 133.49, 129.71, 129.69, 129.64, 129.61, 128.83, 127.86, 127.47, 76.52, 69.84. IR (ATR): 3064 (w), 3030 (w), 2974 (w), 2909 (w), 2369 (w), 2346 (w), 1620 (m), 1602 (m), 1579 (m), 1497 (m), 1474 (m), 1452 (m), 1381 (m), 1325 (m), 1277 (m), 1245 (m), 1183 (m), 1116 (m), 1077 (m), 1027 (m), 982 (m), 943 (m), 760 (s), 693 (s). UV–vis [CH_3CN; λ_{max}, nm (ε, M^{-1} cm^{-1})]: 191 (5580), 209 sh (3148). CD [CH_3CN; θ_{max}, nm (ε_{CD}, M^{-1} cm^{-1})]: 206 (−3.97), 324 (−0.77).

[Cd($\mathbf{1_H}$)$_2$I$_2$]. (Ph-ox)–C_6H_5 ($\mathbf{1_H}$)(0.10 mmol, 22.3 mg), CdI_2 (0.049 mmol, 18.3 mg). Thin needle-like colorless single crystals were obtained after 2 days. Yield: 37.35 mg (0.045 mmol, 92%). ^{1}H NMR (600 MHz, $CDCl_3$) δ/ppm: 8.03 (dd, J = 8.3, 1.3 Hz, 2H), 7.57 (t, J = 7.5 Hz, 1H), 7.47 (dd, J = 8.4, 7.0 Hz, 2H), 7.41–7.32 (m, 2H), 7.35–7.28 (m, 3H), 5.56 (dd, J = 10.2, 7.2 Hz, 1H), 4.80 (t, J = 9.3 Hz, 1H), 4.37 (dd, J = 8.5, 7.2 Hz, 1H). ^{13}C NMR (151 MHz, CD_3CN) δ/ppm: 168.44, 142.37, 133.60, 129.97, 129.66, 129.64, 129.57, 128.84, 128.46, 127.91, 127.26, 76.59, 69.80. IR (ATR): 3063 (w), 3030 (w), 3012 (w), 2973 (w), 2913 (w), 2367 (w), 2346 (w), 1620 (m), 1603 (m), 1579 (m), 1497 (m), 1474 (m), 1452 (m), 1383 (m), 1325 (w), 1245 (m), 1116 (m), 1077 (w), 1026 (w), 984 (w), 943 (m), 760 (s), 693 (s). UV–vis [CH_3CN; λ_{max}, nm (ε, M^{-1} cm^{-1})]: 194 (98 249), 206 sh (61 262), 243 (23 914). CD [CH_3CN; θ_{max}, nm (ε_{CD}, M^{-1} cm^{-1})]: 193 (−0.24), 211 (−11.08), 227 (6.86), 255 (−5.23), 282 (0.79).

[Cd($\mathbf{1_{mA}}$)$_2$I$_2$]. (Ph-ox)–C_6H_4–AlaOMe ($\mathbf{1_{mA}}$)(0.10 mmol, 35.2 mg), CdI_2 (0.049 mmol, 11.0 mg). Thin rod-like colorless single crystals were obtained after 3 days. Yield: 31.9 mg (0.034 mmol, 69%). ^{1}H NMR (600 MHz, $CDCl_3$) δ/ppm: 8.69–8.59 (m, 1H), 8.35–8.26 (m, 1H), 7.63–7.56 (m, 1H), 7.51 (t, J = 7.8 Hz, 2H), 7.41–7.29 (m, 5H), 5.93 (s, 1H), 4.80 (quin., J = 7.3 Hz, 1H), 4.74 (t, J = 9.5 Hz, 1H), 3.79 (s, 3H), 1.68 (d, J = 7.3 Hz, 3H). ^{13}C NMR (151 MHz, $CDCl_3$) δ/ppm: 173.53, 165.18, 133.42, 132.98, 129.27, 129.11, 128.56, 127.51, 126.52, 76.42, 69.26, 52.64, 49.45, 18.07. IR (ATR): 3383 (w), 3006 (w), 1763 (m), 1744 (w), 1726 (w), 1698 (m), 1681 (m), 1646 (m). 1603 (w), 1588 (w), 1567 (w), 1543 (m), 1536 (m), 1517 (w), 1483 (w), 1463 (w), 1379 (w), 1245 (m), 1191 (w), 1163 (w), 1137 (w), 1077 (w), 1018 (w), 982 (w), 962 (w), 933 (w), 874 (w), 848 (w), 783 (m), 773 (m), 753 (w), 736 (m), 727 (m). UV–vis [CH_2Cl_2, c ([Cd($\mathbf{1_{mA}}$)$_2$I$_2$]) = 0.03 mM; λ_{max}, nm (ε_{UV}, M^{-1} cm^{-1})]: 249 (sh, 19 057). CD [CH_2Cl_2, c ([Cd($\mathbf{1_{mA}}$)$_2$I$_2$]) = 0.03 mM; θ_{max}, nm (ε_{CD}, M^{-1} cm^{-1})]: 237 (4.05), 262 (−4.22).

[Co($\mathbf{1_H}$)$_2$Br$_2$]. (Ph-ox)–C_6H_5 ($\mathbf{1_H}$)(0.225 mmol, 50.23 mg), $CoBr_2$ (0.113 mmol, 24.61 mg). Yield: 69.46 mg (0.105 mmol, 93%), blue powder. Thin needle-like blue single crystals were obtained after 2 days. IR (ATR): 3411 (w), 3060 (w), 2995 (w), 2950 (w), 2134 (w), 1746 (w), 1636 (m), 1626 (m), 1603 (w), 1519 (m), 1476 (m), 1407 (m), 1241 (w), 1263 (m), 1144 (w), 1101 (w), 1053 (w), 1021 (w), 969 (w), 768 (w), 721 (s). UV–vis [CH_2Cl_2; λ_{max}, nm (ε_{UV}, M^{-1} cm^{-1})]: 236 (21 649), 279 (−4.07), 314 (2.36), 606 (sh, 306), 621 (sh, 383), 640 (sh, 544), 663 (681). CD [CH_2Cl_2; θ_{max}, nm (ε_{CD}, M^{-1} cm^{-1})]: 253 (2.19), 530 (0.02), 535 (0.02), 585 (−0.026), 652 (0.31), 693 (0.06).

[Co($\mathbf{1_F}$)$_2$Br$_2$]. (Ph-ox)–$p$$C_6H_4$–F ($\mathbf{1_F}$)(0.225 mmol, 54.29 mg), $CoBr_2$ (0.113 mmol, 24.61 mg). Yield: 70.88 mg (0.102 mmol, 90%), blue powder. IR (ATR): 3091 (w), 2928 (w), 1756 (w), 1644 (m), 1629 (m), 1605 (w), 1536 (m), 1497 (w), 1480 (w), 1441 (w), 1416 (w), 1403 (w), 1341 (w), 1329 (w), 1295 (w), 1260 (m), 1252 (m), 1186 (m), 1135 (w), 1126 (m), 1079 (w), 1053 (w), 1038 (w), 1019 (w), 1003 (w), 971 (w), 952 (w), 878 (m), 846 (w), 839 (m), 785 (m), 775 (m), 760 (m), 725 (m), 716 (m). UV–vis [CH_2Cl_2, λ_{max}, nm (ε_{UV}, M^{-1} cm^{-1})]: 248 (23 356), 356 (134), 605 (sh, 241), 622 (sh, 338), 641 (sh, 449), 666 (592), 699 (sh, 333). CD [CH_2Cl_2; θ_{max}, nm (ε_{CD}, M^{-1} cm^{-1})]: 282 (−1.04), 311 (2.25), 603 (0.07), 620 (0.10), 654 (0.21), 693 (0.05).

[Co($\mathbf{1_N}$)$_2$Br$_2$]. (Ph-ox)–$p$$C_6H_4$–$NMe_2$ ($\mathbf{1_N}$)(0.225 mmol, 59.92 mg), $CoBr_2$ (0.113 mmol, 24.61 mg). Yield: 75.23 mg (0.102 mmol, 89%), green powder. Green plate-like single crystals were obtained after 2 days. IR (ATR): 3062 (w), 2932 (w), 2678 (w), 2139 (w), 1618 (s), 1606 (s), 1551 (s), 1547 (s), 1502 (m), 1457 (m), 1396 (s), 1371 (m), 1252 (m), 1334 (w), 1308 (w), 1256 (w), 1221 (s), 1200 (s), 1146 (m), 1139 (m), 1088 (m), 1021 (w), 969 (m), 952 (m), 924 (m), 850 (m), 773 (m), 721 (s). UV–vis [CH_2Cl_2; λ_{max}, nm (ε_{UV}, M^{-1} cm^{-1})]: 316 (sh, 20 032), 365 (66 650), 433 (sh, 141), 606 (sh, 165), 621 (sh, 238), 642 (sh, 364), 667 (542), 700 (517), 726 (sh, 306). CD [CH_2Cl_2; θ_{max}, nm (ε_{CD}, M^{-1} cm^{-1})]: 255 (2.01), 271 (−1.24), 335 (6.41), 372 (2.99), 426 (0.14), 596 (−0.06), 605 (−0.05), 652 (0.13).

[Co($\mathbf{1_P}$)$_2$Cl$_2$]·CH$_3$CN. (Ph-ox)–$C_{16}H_9$ ($\mathbf{1_P}$)(0.113 mmol, 39.31 mg), $CoCl_2{\cdot}6H_2O$ (0.056 mmol, 13.33 mg). Several green dodecahedron-like single crystals were picked out of a white, cotton like fibrous solid after 2 days.

[Co($\mathbf{1_P}$)$_2$Br$_2$]. (Ph-ox)–$C_{16}H_9$ ($\mathbf{1_P}$)(0.113 mmol, 39.31 mg), $CoBr_2$ (0.056 mmol, 12.30 mg). Yield: 49.14 mg (0.53 mmol, 95%), green powder. Green needle-like single crystals were obtained after 2 days. IR (ATR): 3323 (w), 3062 (w), 2984 (w), 2954 (w), 2924 (w), 2147 (w), 1618 (m), 1599 (m), 1588 (m), 1567 (w), 1536 (w), 1519 (w), 1476 (w), 1401 (w), 1323 (w), 1210 (w), 1262 (w), 1234 (w), 1210 (w), 1169 (w), 1157 (w), 1116 (w), 1108 (w), 1072 (w), 1053 (w), 1025 (w), 1001 (w), 971 (w), 876 (m), 855 (m), 826 (w), 775 (m), 747 (w), 7267 (s). UV–vis [CH_2Cl_2; λ_{max}, nm (ε_{UV}, M^{-1} cm^{-1})]: 239 (sh, 85 244), 243 (87 812), 274 (sh, 48 451), 284 (63 251), 352 (54 705), 363 (sh, 44 786), 384 (sh, 17 633), 601 (sh, 371), 638 (sh, 624), 660 (773), 700 (sh, 208). CD [CH_2Cl_2; θ_{max}, nm (ε_{CD}, M^{-1} cm^{-1})]: 246 (11.83), 260 (−6.12), 273 (4.49), 285 (−12.29), 298 (1.71), 352

(16.92), 365 (sh, 14.73), 384 (3.24), 406 (−4.47), 532 (0.03), 601 (0.48), 616 (0.49), 657 (0.77).

[Co($\mathbf{1_{mA}}$)$_2$Br$_2$]. (Ph-ox)–*m*C$_6$H$_4$–AlaOMe ($\mathbf{1_{mA}}$) (0.113 mmol, 39.61 mg), CoBr$_2$ (0.056 mmol, 12.30 mg). Yield: 42.57 mg (0.46 mmol, 82%), blue powder. Blue rod-like single crystals were obtained after 2 days. IR (ATR): 3356 (w), 3319 (w), 2948 (w), 2363 (w), 1744 (m), 1672 (m), 1638 (m), 1543 (m), 1519 (m), 1450 (w), 1388 (w), 1347 (w), 1303 (w), 1265 (w), 1211 (m), 1163 (m), 1057 (w), 980 (w), 939 (w), 762 (w), 697 (m). UV–vis [CH$_2$Cl$_2$; λ_{max}, nm (ε_{UV}, M^{-1} cm^{-1})]: 248 (sh, 24 013), 602 (sh, 313), 637 (sh, 550), 662 (693). CD [CH$_2$Cl$_2$; θ_{max}, nm (ε_{CD}, M^{-1} cm^{-1})]: 239 (24.65), 280 (−4.89), 309 (4.15), 664 (0.66).

[Co($\mathbf{1_{mA}}$*)$_2$Br$_2$]. ((*R*)-Ph-ox)–*m*C$_6$H$_4$–AlaOMe ($\mathbf{1_{mA}}$*) (0.07 mmol, 24.65 mg), CoBr$_2$ (0.035 mmol, 8.66 mg). Yield: 32.48 mg (0.034 mmol, 98%), blue powder. IR (ATR): 3541 (w), 3319 (w), 3030 (w), 2954 (w), 2936 (w), 2924 (w), 2855 (w), 2376 (w), 1737 (m), 1643 (m), 1620 (sh m), 1579 (w), 1528 (m), 1454 (m), 1439 (m), 1377 (w), 1347 (w), 1301 (w), 1213 (m), 1167 (m), 1133 (m), 1049 (m), 980 (m), 960 (m), 937 (m), 883 (w), 846 (w), 820 (w), 759 (m), 731 (m), 697 (s). UV–vis [CH$_2$Cl$_2$; λ_{max}, nm (ε_{UV}, M^{-1} cm^{-1})]: 254 (sh, 18 484), 603 (sh, 239), 640 (sh, 431), 664 (sh, 546), 664 (406), 699 (sh, 204). CD [CH$_2$Cl$_2$; θ_{max}, nm (ε_{CD}, M^{-1} cm^{-1})]: 240 (−2.43), 282 (3.46), 317 (−1.21), 660 (−0.34).

[Co($\mathbf{1_{m2A}}$)$_2$Br$_2$]. (Ph-ox)–*m*C$_6$H$_4$–(AlaOMe)$_2$ ($\mathbf{1_{m2A}}$) (0.07 mmol, 33.71 mg), CoBr$_2$ (0.035 mmol, 8.66 mg). Yield: 29.57 mg (0.025 mmol, 71%), blue powder. Blue rod-like single crystals were obtained after 2 days. IR (ATR): 3537 (w), 3355 (w), 3314 (w), 2961 (w), 2365 (w), 2085 (w), 1744 (m), 1671 (m), 1646 (m), 1618 (w), 1586 (m), 1543 (m), 1521 (m), 1450 (m), 1437 (m), 1387 (m), 1347 (m), 1301 (m), 1260 (m), 1211 (s), 1161 (m), 1096 (m), 1047 (m), 1018 (m), 980 (m), 939 (m), 798 (s), 762 (m), 697 (m). UV–vis [CH$_2$Cl$_2$; λ_{max}, nm (ε_{UV}, M^{-1} cm^{-1})]: 254 (sh, 19 000), 602 (sh, 174), 642 (sh, 314), 664 (386), 698 (sh, 207), 727 (sh, 122). CD [CH$_2$Cl$_2$; θ_{max}, nm (ε_{CD}, M^{-1} cm^{-1})]: 241 (4.14), 278 (−1.41), 314 (0.99), 596 (−0.13), 657 (0.72).

[Co($\mathbf{1_{m2A}}$*)$_2$Br$_2$]. ((*R*)-Ph-ox)–*m*C$_6$H$_4$–(AlaOMe)$_2$ ($\mathbf{1_{mA}}$*) (0.07 mmol, 33.71 mg), CoBr$_2$ (0.035 mmol, 8.66 mg). Yield: 32.36 mg (0.027 mmol, 78%), blue powder. IR (ATR): 3371 (sh w), 3065 (w), 2987 (w), 2952 (w), 2093(w), 1733 (m), 1647 (s), 1593 (m), 1528 (m), 1450 (m), 1381 (w), 1342 (sh m), 1303 (w), 1246 (sh m), 1215 (m), 1159 (m), 1126 (m), 1052 (m), 982 (m), 937 (w), 849 (w), 734 (m), 697 (m). UV–vis [CH$_2$Cl$_2$; λ_{max}, nm (ε_{UV}, M^{-1} cm^{-1})]: 256 (sh, 17 301), 603 (sh, 215), 644 (sh, 425), 667 (529), 698 (sh, 289), 734 (sh, 130). CD [CH$_2$Cl$_2$, θ_{max}, nm (ε_{CD}, M^{-1} cm^{-1})]: 241 (19.83), 286 (sh, 2.8), 322 (−1.44), 571 (−0.05), 660 (−0.32).

[Co(BOX1)Br$_2$]. (−)-2,2′-Isopropylidenebis[(4*S*)-4-phenyl-2-oxazoline] (**BOX1**) (0.009 mmol, 3.00 mg), CoBr$_2$ (0.009 mmol, 1.96 mg). Dark blue, needle-like crystals were obtained from a CH$_2$Cl$_2$ stock solution for CD spectroscopy after 5 days. UV–vis [CH$_2$Cl$_2$; λ_{max}, nm (ε_{UV}, M^{-1} cm^{-1})]: 228 (10 327), 298 (2607), 546 (sh, 170), 571 (295), 648 (582). CD [CH$_2$Cl$_2$; θ_{max}, nm (ε_{CD}, M^{-1} cm^{-1})]: 246 (1.89), 261 (1.94), 291 (2.51), 311 (−0.34), 335 (0.41), 543 (0.30), 566 (0.42), 637 (−0.26).

[Co(BOX2)Br$_2$]. (+)-2,2′-Isopropylidenebis[(4*R*)-4-benzyl-2-oxazoline] (**BOX2**) (0.009 mmol, 3.26 mg), CoBr$_2$ (0.009 mmol, 1.96 mg). Dark blue, rhomb-like crystals were obtained from a CH$_2$Cl$_2$ stock solution for CD spectroscopy after 5 days. UV–vis [CH$_2$Cl$_2$; λ_{max}, nm (ε_{UV}, M^{-1} cm^{-1})]: 362 (36), 549 (sh, 146), 572 (263), 644 (263). CD [CH$_2$Cl$_2$; θ_{max}, nm (ε_{CD}, M^{-1} cm^{-1})]: 541 (−0.17), 566 (−0.25), 624 (0.27).

X-ray single crystal diffraction

X-ray intensity data were collected on Xcalibur or XtaLAB Oxford diffraction diffractometers using monochromatic Cu-Kα radiation (λ = 1.54184 Å). The data collected on laboratory diffractometers were processed (cell determination and data reduction) by the CrysalisPro program.[58] All structures were solved by the program SXELXT[59] and refined according to the least-squares procedure (F^2 on all data) by the program SHELXL.[60] Basic experimental data are given in Table S4 of SI. The absolute configurations of investigated compounds were known from the synthetic procedures, so the Friedel opposite reflections were not measured. All non-hydrogen atoms are refined in the anisotropic model of atomic displacement parameters (ADP). One ligand in one of the three symmetry independent metal complexes in [Zn($\mathbf{1_N}$)$_2$Br$_2$] had strongly elongated ADPs, so strong rigid-group restraints were applied to all ligand's atoms and its terminal phenyl group was treated in the ideal hexagonal geometry. Less strong rigid body restraints were used for other two symmetry independent complexes in this structure. For [Zn($\mathbf{1_H}$)$_2$I$_2$] more accurate Gaussian absorption correction with determination of the crystal faces was applied, which leaded to good final *R*-value and good residual electron density. Only empirical absorption correction was applied to [Cd($\mathbf{1_H}$)$_2$I$_2$], which is possible a reason for the less accurate structure (high *R*-value) and less accurate residual electron density (high peak/minimum). Nevertheless, the [Cd($\mathbf{1_H}$)$_2$I$_2$] was found to be isostructural with [Zn($\mathbf{1_H}$)$_2$Br$_2$], [Zn($\mathbf{1_H}$)$_2$I$_2$], [Cd($\mathbf{1_H}$)$_2$Br$_2$] and [Co($\mathbf{1_H}$)$_2$Br$_2$] complexes, which were determined with high accuracy (Table S4). For [Cd($\mathbf{1_H}$)$_2$I$_2$] and for $\mathbf{1_{mA}}$* the extinction was refined by standard procedure in SHELXL.[60] In [Co($\mathbf{1_P}$)$_2$Cl$_2$] and [Co($\mathbf{1_P}$)$_2$Br$_2$] the pyrene units were treated as rigid groups with geometry taken from the Idealized Molecular Geometry Library.[61] Some atoms in [Co($\mathbf{1_P}$)$_2$Br$_2$] show large and elongated ADPs, but because they are neighbouring atoms of the same pyrene moiety, they are the consequence of a dynamic disorder of the whole pyrene group. Large ADPs for C atoms in this group are also the reason for the large Hirshfeld differences for its C–C bonds. For [Zn($\mathbf{1_{m2A}}$)$_2$Br$_2$] the analysis of the intensity data revealed a twined sample with two-axis twinning law described in Table S4 of SI. Refinement with twinning significantly improved the quality of the refined twinned volume fractions of 0.81 and 0.19 (Table S4). The [Co($\mathbf{1_{m2A}}$)$_2$Br$_2$] was also tested for the same twinning low (assumed to be present due to same isostructural structure as [Zn($\mathbf{1_{m2A}}$)$_2$Br$_2$] and due to relatively high R_{init} value for [Co($\mathbf{1_{m2A}}$)$_2$Br$_2$] data set), but the refined volume fraction of one of the components turned out to be negligible. The treatments of hydrogen atoms in all structures

are described in Table S4 of SI. Generally, the H atoms bonded to carbon were treated in the SHELXL riding model for CH, CH_2 and CH_3 groups, while the treatment of H atoms bonded to N atoms depended on the quality of the data set: for a good data they were refined, for less accurate data the they were refined and N–H distance restraints were used or for poor quality data sets they were treated in the SHELXL riding model for sp^2 NH group. For all compounds in which solvent accessible voids greater than 50 Å^3 were found in their structures the electron densities from these areas was included by the SQUEEZE procedure of program PLATON.[62] The CCDC 2489428–2489446 contain the supplementary crystallographic data for this paper.

Computational details

The starting geometries for bromide and nitrate metal complexes with non-alanine ligands ($\mathbf{1_H}$, $\mathbf{1_F}$, $\mathbf{1_N}$) were generated by applying a CREST/CENSO protocol[63] to the geometry obtained from the $[Zn(\mathbf{1_H})_2(NO_3)_2]$ crystal structure. From the CENSO structures, starting geometries of bromide analogues were derived by switching R substituents, the nitrate anions with bromides, and setting the M–Br bond lengths to the lengths found in their respective crystal structures. The IIa* starting geometry was constructed from the crystal structure of the zinc metal complex found in literature (CCDC code ETUVIY).[54]

Bromide zinc complexes of alanine derivatives $\mathbf{1_{mA}}$, $\mathbf{1_{mA}}$*, $\mathbf{1_{m2A}}$, and $\mathbf{1_{m2A}}$* were studied using CREST to identify the most relevant geometries at room temperature in chloroform ($CHCl_3$). The initial geometries for the CREST runs were generated with Avogadro and prepared in both parallel and antiparallel configurations. Since both sets of input geometries produced conformers with approximately the same geometries and energies, to simplify the calculations, only the structures from the parallel runs were considered as inputs for subsequent DFT optimization. For each ligand in the DFT optimization, only structures within 3 kcal mol^{-1} of the lowest-energy conformer (corresponding to a 99% probability of being populated at room temperature) or higher-energy geometries that displayed interesting hydrogen-bonding motifs were selected. Additionally, geometries with specific hydrogen bonding motifs that were not obtained from CREST were constructed from other conformers and used as inputs in the next calculation step.

The geometries of representative conformers of both non-alanine and alanine derivative complexes, selected using CREST, served as starting points for DFT geometry optimizations. These optimizations employed the efficient M05-2X/6-31+G(d)/LanL2DZ+ECP model, which has been shown to accurately reproduce geometries, dipole moments, and homolytic bond energies in various metal complexes,[64,65] consistent with our comparative analysis of other DFT approaches for similar systems.[66] To account for solvent effects, the implicit SMD solvation model (ε = 4.7113) for chloroform and acetonitrile (ε = 35.688) was included during geometry optimization, as in our earlier studies.[67] Thermal corrections were obtained from frequency calculations, ensuring that all reported values correspond to Gibbs free energy differences at room temperature. All calculations were performed with Gaussian 16.[68] The DFT optimized geometries can be found in non_alanine_derivatives.xyz and alanine_derivatives.xyz, readable by the Mercury program (version 3.3 or later),[69] and related data are collected in Tables S8–S17.

Author contributions

M. B. and E. S. prepared and characterized the ligands. M. B. prepared and characterized the complexes, performed the spectroscopic experiments and wrote the manuscript draft. B. P. performed the crystallographic studies. M. B. and T. R. performed the computational studies. Z. K. supervised the spectroscopic experiments. Z. Š. performed the X-ray diffraction experiments on single crystals. R. V. supervised the computational studies. S. I. K. conceived the study, supervised the experiments and finalized the manuscript. All authors have approved the manuscript.

Conflicts of interest

There are no conflicts to declare.

Data availability

Data for this article have been included as part of the supplementary information (SI). Supplementary information: compounds overview, NMR spectra, overlapped NMR spectra, UV-Vis spectra, CD spectra, mass spectra, HRMS spectra, IR spectra, powder diffraction data and calculation data. See DOI: https://doi.org/10.1039/d5dt02399h.

CCDC 2489428–2489446 contain the supplementary crystallographic data for this paper.[70a–s]

Acknowledgements

This work was supported by CAT Pharma (KK.01.1.1.04.0013), a project co-financed by the Croatian Government and the European Union through the European Regional Development Fund – the Competitiveness and Cohesion Operational Program; and Cage Cat (IP-2022-10-8456), a project financed by the Croatian Science Foundation. M. B. acknowledges the Croatian Science Foundation for a doctoral scholarship (DOK-2021–02-7366). We thank Dr Lucija Hok, Dr Tana Tandarić, Dr Natalija Pantalon Juraj and Dr Saša Opačak for helpful discussions.

References

1 M. M. Coelho, C. Fernandes, F. Remião and M. E. Tiritan, Enantioselectivity in Drug Pharmacokinetics and Toxicity:

Pharmacological Relevance and Analytical Methods, *Molecules*, 2021, **26**, 3113.
2 H.-U. Blaser, B. Pugin and F. Spindler, Asymmetric Hydrogenation, in *Organometallics as Catalysts in the Fine Chemical Industry*, ed. M. Beller and H.-U. Blaser, Springer Berlin Heidelberg, Berlin, Heidelberg, 2012, pp. 65–102.
3 L. Lloyd, *Handbook of Industrial Catalysts*, Springer US, Boston, MA, 2011.
4 B. Shen, Y. Kim and M. Lee, Supramolecular Chiral 2D Materials and Emerging Functions, *Adv. Mater.*, 2020, **32**, 1905669.
5 D. B. Amabilino and J. Veciana, Supramolecular Chiral Functional Materials, in *Supramolecular Chirality*, ed. M. Crego-Calama and D. N. Reinhoudt, Springer Berlin Heidelberg, Berlin, Heidelberg, 2006, pp. 253–302.
6 X. Zhang, J. Yin and J. Yoon, Recent advances in development of chiral fluorescent and colorimetric sensors, *Chem. Rev.*, 2014, **114**, 4918–4959.
7 Z.-H. Yan, D. Li and X.-B. Yin, Review for chiral-at-metal complexes and metal-organic framework enantiomorphs, *Sci. Bull.*, 2017, **62**, 1344–1354.
8 P. S. Steinlandt, L. Zhang and E. Meggers, Metal Stereogenicity in Asymmetric Transition Metal Catalysis, *Chem. Rev.*, 2023, **123**, 4764–4794.
9 Z.-Y. Cao, W. D. G. Brittain, J. S. Fossey and F. Zhou, Recent advances in the use of chiral metal complexes with achiral ligands for application in asymmetric catalysis, *Catal. Sci. Technol.*, 2015, **5**, 3441–3451.
10 J. Crassous, Transfer of chirality from ligands to metal centers: recent examples, *Chem. Commun.*, 2012, **48**, 9687–9695.
11 G. C. Hargaden and P. J. Guiry, Recent applications of oxazoline-containing ligands in asymmetric catalysis, *Chem. Rev.*, 2009, **109**, 2505–2550.
12 F. Freire, J. M. Seco, E. Quiñoá and R. Riguera, in *Hierarchical Macromolecular Structures: 60 Years after the Staudinger Nobel Prize II*, ed. V. Percec, Springer International Publishing, Cham, 2013.
13 R. Horikoshi and T. Mochida, Metal complexes of 4,4′-dipyridyldisulfide—structural diversity derived from a twisted ligand with axial chirality, *Coord. Chem. Rev.*, 2006, **250**, 2595–2609.
14 J. Dong, Y. Liu and Y. Cui, Supramolecular Chirality in Metal–Organic Complexes, *Acc. Chem. Res.*, 2021, **54**, 194–206.
15 J. Crassous, Chiral transfer in coordination complexes: towards molecular materials, *Chem. Soc. Rev.*, 2009, **38**, 830–845.
16 R. S. Cahn, C. K. Ingold and V. Prelog, Specification of Molecular Chirality, *Angew. Chem., Int. Ed. Engl.*, 1966, **5**, 385–415.
17 N. Pantalon Juraj and S. I. Kirin, Inorganic stereochemistry: Geometric isomerism in bis-tridentate ligand complexes, *Coord. Chem. Rev.*, 2021, **445**, 214051.
18 N. Pantalon Juraj, M. Krklec, T. Novosel, B. Perić, R. Vianello, S. Raić-Malić and S. I. Kirin, Copper(II) and zinc(II) complexes of mono- and bis-1,2,3-triazole-substituted heterocyclic ligands, *Dalton Trans.*, 2020, **49**, 9002–9015.
19 J. M. Lassaletta, *Atropisomerism and Axial Chirality*, World Scientific (Europe), 2019.
20 M. Raynal, P. Ballester, A. Vidal-Ferran and P. W. N. M. Van Leeuwen, Supramolecular catalysis. Part 1: non-covalent interactions as a tool for building and modifying homogeneous catalysts, *Chem. Soc. Rev.*, 2014, **43**, 1660–1733.
21 R. S. Herrick, R. M. Jarret, T. P. Curran, D. R. Dragoli, M. B. Flaherty, S. E. Lindyberg, R. A. Slate and L. C. Thornton, Ordered conformations in bis(amino acid) derivatives of 1,1′-ferrocenedicarboxylic acid, *Tetrahedron Lett.*, 1996, **37**, 5289–5292.
22 T. Moriuchi and T. Hirao, Highly ordered structures of peptides by using molecular scaffolds, *Chem. Soc. Rev.*, 2004, **33**, 294–301.
23 S. I. Kirin, H.-B. Kraatz and N. Metzler-Nolte, Systematizing structural motifs and nomenclature in 1,*n*′-disubstituted ferrocene peptides, *Chem. Soc. Rev.*, 2006, **35**, 348.
24 R. Connon, B. Roche, B. V. Rokade and P. J. Guiry, Further Developments and Applications of Oxazoline-Containing Ligands in Asymmetric Catalysis, *Chem. Rev.*, 2021, **121**, 6373–6521.
25 T. Lorson, M. M. Lübtow, E. Wegener, M. S. Haider, S. Borova, D. Nahm, R. Jordan, M. Sokolski-Papkov, A. V. Kabanov and R. Luxenhofer, Poly(2-oxazoline)s based biomaterials: A comprehensive and critical update, *Biomaterials*, 2018, **178**, 204–280.
26 M. Gómez, G. Muller and M. Rocamora, Coordination chemistry of oxazoline ligands, *Coord. Chem. Rev.*, 1999, **193–195**, 769–835.
27 T. P. Yoon and E. N. Jacobsen, Privileged chiral catalysts, *Science*, 2003, **299**, 1691–1693.
28 J. Shen, N. Ikeda, W. Bi, K. Satoh, M. Kamigaito and Y. Okamoto, Helix-sense-selective copolymerization of triphenylmethyl methacrylate with chiral 2-isopropenyl-4-phenyl-2-oxazoline, *J. Polym. Sci., Part A: Polym. Chem.*, 2019, **57**, 441–447.
29 Y. Chatani, T. Kobatake, H. Tadokoro and R. Tanaka, Structural studies of poly(ethylenimine). 2. Double-stranded helical chains in the anhydrate, *Macromolecules*, 1982, **15**, 170–176.
30 E. Yashima, H. Goto and Y. Okamoto, Metal-Induced Chirality Induction and Chiral Recognition of Optically Active, Regioregular Polythiophenes, *Macromolecules*, 1999, **32**, 7942–7945.
31 G. Mugesh, H. B. Singh, R. P. Patel and R. J. Butcher, Synthesis and Structural Characterization of Monomeric Selenolato Complexes of Zinc, Cadmium, and Mercury, *Inorg. Chem.*, 1998, **37**, 2663–2669.
32 M. Seitz, A. Kaiser, S. Stempfhuber, M. Zabel and O. Reiser, Helical, Nonracemic Inorganic–Organic Hybrid Polymers of Cadmium Halides with Pentadentate Bis(oxazoline) Ligands, *J. Am. Chem. Soc.*, 2004, **126**, 11426–11427.
33 C. Mazet and L. H. Gade, [Bis(oxazolinyl)pyrrole]palladium Complexes as Catalysts in Heck- and Suzuki-Type C–C

Coupling Reactions, *Eur. J. Inorg. Chem.*, 2003, **2003**, 1161–1168.

34 H. Wang, N. Li, J. Zhang and X. Wan, Synthesis and Properties of a Novel Pyridineoxazoline Containing Optically Active Helical Polymer as a Catalyst Ligand for Asymmetric Diels–Alder Reaction, *Chirality*, 2015, **27**, 523–531.

35 C. C. Sorensen and F. A. Leibfarth, Stereoselective Helix-Sense-Selective Cationic Polymerization of N-Vinylcarbazole Using Chiral Lewis Acid Catalysis, *J. Am. Chem. Soc.*, 2022, **144**, 8487–8492.

36 C. Provent, S. Hewage, G. Brand, L. J. Charbonnière, A. F. Williams and G. Bernardinelli, Enantioselective Formation of Double and Triple Helicates of Silver(I): The Role of Stacking Interactions, *Angew. Chem., Int. Ed. Engl.*, 1997, **36**, 1287–1289.

37 M. Seitz, S. Stempfhuber, M. Zabel, M. Schütz and O. Reiser, Helical Chirality in Pentacoordinate Zinc Complexes—Selective Access to Both Pseudoenantiomers with One Ligand Configuration, *Angew. Chem., Int. Ed.*, 2005, **44**, 242–245.

38 J. Barberá, E. Cavero, M. Lehmann, J.-L. Serrano, T. Sierra and J. T. Vázquez, Supramolecular Helical Stacking of Metallomesogens Derived from Enantiopure and Racemic Polycatenar Oxazolines, *J. Am. Chem. Soc.*, 2003, **125**, 4527–4533.

39 S. R. Nam, H.-J. Kim, S. Sakamoto, K. Yamaguchi and J.-I. Hong, Unidirectional helical assembly via triple hydrogen bonds between chiral tris(oxazoline) and achiral tris (imidazoline), *Tetrahedron Lett.*, 2004, **45**, 1339–1342.

40 Y.-Q. Huang and W.-Y. Sun, Coordination supramolecules with oxazoline-containing ligands, *CrystEngComm*, 2018, **20**, 6109–6121.

41 C.-L. Liu, L.-P. Zhou, D. Tripathy and Q.-F. Sun, Self-assembly of stable luminescent lanthanide supramolecular M4L6 cages with sensing properties toward nitroaromatics, *Chem. Commun.*, 2017, **53**, 2459–2462.

42 Y. Zhao, L. Luo, C. Liu, M. Chen and W.-Y. Sun, Helical silver(I) coordination polymer with oxazoline-containing ligand: Structure, non-linear and ferroelectric property, *Inorg. Chem. Commun.*, 2011, **14**, 1145–1148.

43 H.-W. Kuai, X.-C. Cheng, D.-H. Li, T. Hu and X.-H. Zhu, Syntheses, characterization and properties of silver, copper and palladium complexes from bis(oxazoline)-containing ligands, *J. Solid State Chem.*, 2015, **228**, 65–75.

44 H. Y. Lee, J. Park, M. S. Lah and J.-I. Hong, A hamburger-shaped helical stacking of disk-shaped ligands mediated by silver(II) ions, *Chem. Commun.*, 2007, 5013–5015.

45 S. Hiraoka, E. Okuno, T. Tanaka, M. Shiro and M. Shionoya, Ranging Correlated Motion (1.5 nm) of Two Coaxially Arranged Rotors Mediated by Helix Inversion of a Supramolecular Transmitter, *J. Am. Chem. Soc.*, 2008, **130**, 9089–9098.

46 D. A. Evans, K. A. Woerpel and M. J. Scott, 'Bis(oxazolines)' as Ligands for Self-Assembling Chiral Coordination Polymers— Structure of a Copper(I) Catalyst for the Enantioselective Cyclopropanation of Olefins, *Angew. Chem., Int. Ed. Engl.*, 1992, **31**, 430–432.

47 M. Durini, E. Russotto, L. Pignataro, O. Reiser and U. Piarulli, SupraBox: Chiral Supramolecular Oxazoline Ligands, *Eur. J. Org. Chem.*, 2012, 5451–5461.

48 M. Bakija, B. Perić and S. I. Kirin, Oxazoline amino acid bioconjugates: one-pot synthesis and analysis of supramolecular interactions, *New J. Chem.*, 2024, 8702–8719.

49 M. Bakija, S. Opačak, B. Perić, S. Chakrabortty, A. Dell'Acqua, E. Baráth, J. G. De Vries, S. Tin and S. I. Kirin, Supramolecular bidentate rhodium(I) or iridium (I) phosphine and oxazoline amino acid bioconjugates as selective catalysts for enantioselective reactions, *Dalton Trans.*, 2025, 1021–1037.

50 B. Breit, Supramolecular Approaches to Generate Libraries of Chelating Bidentate Ligands for Homogeneous Catalysis, *Angew. Chem., Int. Ed.*, 2005, **44**, 6816–6825.

51 G. Xu, Q. Luo, S. Eibauer, A. F. Rausch, S. Stempfhuber, M. Zabel, H. Yersin and O. Reiser, Palladium(II)- and platinum(II)phenyl-2,6-bis(oxazole) pincer complexes: Syntheses, crystal structures, and photophysical properties, *Dalton Trans.*, 2011, **40**, 8800–8806.

52 S. Đaković, L. Liščić-Tumir, S. I. Kirin, V. Vinković, Z. Raza, A. Šuste and V. Šunjić, Enantioselectivity in cyclo-propanation catalysed by Cu(I) complexes increased by π stacking of two monodentate oxazoline ligands, *J. Mol. Catal. A: Chem.*, 1997, **118**, 27–31.

53 L. J. Farrugia, ORTEP-3 for Windows - a version of ORTEP-III with a Graphical User Interface (GUI), *J. Appl. Crystallogr.*, 1997, **30**, 565–565.

54 T. M. Barclay, I. Del Río, R. A. Gossage and S. M. Jackson, Oxazoline chemistry—Part IV: Synthesis and characterization of oxazoline complexes of the zinc halides, *Can. J. Chem.*, 2003, **81**, 1482–1491.

55 R. A. Gossage, P. N. Yadav, T. D. MacInnis, J. W. Quail and A. Decken, Zinc halide oxazoline complexes—The quest for structural diversity, *Can. J. Chem.*, 2009, **87**, 368–379.

56 M.-G. Alexandru, T. Cirkovic Velickovic, M. Krstic, M.-M. Hrubaru and C. Draghici, Two complexes of Co(II) and Pd(II) formed in reaction with a mono-oxazoline derivative. Spectroscopic characterization and cytotoxic evaluation, *J. Mol. Struct.*, 2013, **1041**, 55–60.

57 N. Pantalon Juraj, T. Tandarić, V. Tadić, B. Perić, D. Moreth, U. Schatzschneider, A. Brozovic, R. Vianello and S. I. Kirin, Tuning the coordination properties of chiral pseudopeptide bis(2-picolyl)amine and iminodiacetamide ligands in Zn(II) and Cu(II) complexes, *Dalton Trans.*, 2022, **51**, 17008–17021.

58 *CrysAlisPro (Version 1.171.39.46)*, Rigaku Oxford Diffraction Ltd, Yarnton, Oxfordshire, England, 2018.

59 G. M. Sheldrick, SHELXT – Integrated space-group and crystal-structure determination, *Acta Crystallogr., Sect. A: Found. Adv.*, 2015, **71**, 3–8.

60 G. M. Sheldrick, Crystal structure refinement with SHELXL, *Acta Crystallogr., Sect. C: Struct. Chem.*, 2015, **71**, 3–8.

61 I. A. Guzei, An idealized molecular geometry library for refinement of poorly behaved molecular fragments with constraints, *J. Appl. Crystallogr.*, 2014, **47**, 806–809.
62 A. L. Spek, PLATON SQUEEZE: a tool for the calculation of the disordered solvent contribution to the calculated structure factors, *Acta Crystallogr., Sect. C: Struct. Chem.*, 2015, **71**, 9–18.
63 S. Grimme, C. Bannwarth, S. Dohm, A. Hansen, J. Pisarek, P. Pracht, J. Seibert and F. Neese, Fully Automated Quantum-Chemistry-Based Computation of Spin–Spin-Coupled Nuclear Magnetic Resonance Spectra, *Angew. Chem., Int. Ed.*, 2017, **56**, 14763–14769.
64 C. J. Cramer and D. G. Truhlar, Density functional theory for transition metals and transition metal chemistry, *Phys. Chem. Chem. Phys.*, 2009, **11**, 10757.
65 E. A. Amin and D. G. Truhlar, Zn Coordination Chemistry: Development of Benchmark Suites for Geometries, Dipole Moments, and Bond Dissociation Energies and Their Use To Test and Validate Density Functionals and Molecular Orbital Theory, *J. Chem. Theory Comput.*, 2008, **4**, 75–85.
66 Đ. Škalamera, E. Sanders, R. Vianello, A. Maršavelski, A. Pevec, I. Turel and S. I. Kirin, Synthesis and characterization of ML and ML2 metal complexes with amino acid substituted bis(2-picolyl)amine ligands, *Dalton Trans.*, 2016, **45**, 2845–2858.
67 N. Pantalon Juraj, G. I. Miletić, B. Perić, Z. Popović, N. Smrečki, R. Vianello and S. I. Kirin, Stereochemistry of Hexacoordinated Zn(II), Cu(II), Ni(II), and Co(II) Complexes with Iminodiacetamide Ligands, *Inorg. Chem.*, 2019, **58**, 16445–16457.
68 M. J. Frisch, G. W. Trucks, H. B. Schlegel, G. E. Scuseria, M. A. Robb, J. R. Cheeseman, G. Scalmani, V. Barone, G. A. Petersson, H. Nakatsuji, X. Li, M. Caricato, A. V. Marenich, J. Bloino, B. G. Janesko, R. Gomperts, B. Mennucci, H. P. Hratchian, J. V. Ortiz, A. F. Izmaylov, J. L. Sonnenberg, D. Williams-Young, F. Ding, F. Lipparini, F. Egidi, J. Goings, B. Peng, A. Petrone, T. Henderson, D. Ranasinghe, V. G. Zakrzewski, J. Gao, N. Rega, G. Zheng, W. Liang, M. Hada, M. Ehara, K. Toyota, R. Fukuda, J. Hasegawa, M. Ishida, T. Nakajima, Y. Honda, O. Kitao, H. Nakai, T. Vreven, K. Throssell, J. A. Montgomery Jr., J. E. Peralta, F. Ogliaro, M. J. Bearpark, J. J. Heyd, E. N. Brothers, K. N. Kudin, V. N. Staroverov, T. A. Keith, R. Kobayashi, J. Normand, K. Raghavachari, A. P. Rendell, J. C. Burant, S. S. Iyengar, J. Tomasi, M. Cossi, J. M. Millam, M. Klene, C. Adamo, R. Cammi, J. W. Ochterski, R. L. Martin, K. Morokuma, O. Farkas, J. B. Foresman and D. J. Fox, *Gaussian 16 Revision C.01*, 2016.
69 C. F. Macrae, I. Sovago, S. J. Cottrell, P. T. A. Galek, P. McCabe, E. Pidcock, M. Platings, G. P. Shields, J. S. Stevens, M. Towler and P. A. Wood, Mercury 4.0: from visualization to analysis, design and prediction, *J. Appl. Crystallogr.*, 2020, **53**, 226–235.
70 (*a*) CCDC 2489428: Experimental Crystal Structure Determination, 2025, DOI: 10.5517/ccdc.csd.cc2pkg4w.; (*b*) CCDC 2489429: Experimental Crystal Structure Determination, 2025, DOI: 10.5517/ccdc.csd.cc2pkg5x; (*c*) CCDC 2489430: Experimental Crystal Structure Determination, 2025, DOI: 10.5517/ccdc.csd.cc2pkg6y; (*d*) CCDC 2489431: Experimental Crystal Structure Determination, 2025, DOI: 10.5517/ccdc.csd.cc2pkg7z; (*e*) CCDC 2489432: Experimental Crystal Structure Determination, 2025, DOI: 10.5517/ccdc.csd.cc2pkg80; (*f*) CCDC 2489433: Experimental Crystal Structure Determination, 2025, DOI: 10.5517/ccdc.csd.cc2pkg91; (*g*) CCDC 2489434: Experimental Crystal Structure Determination, 2025, DOI: 10.5517/ccdc.csd.cc2pkgb2; (*h*) CCDC 2489435: Experimental Crystal Structure Determination, 2025, DOI: 10.5517/ccdc.csd.cc2pkgc3; (*i*) CCDC 2489436: Experimental Crystal Structure Determination, 2025, DOI: 10.5517/ccdc.csd.cc2pkgd4; (*j*) CCDC 2489437: Experimental Crystal Structure Determination, 2025, DOI: 10.5517/ccdc.csd.cc2pkgf5; (*k*) CCDC 2489438: Experimental Crystal Structure Determination, 2025, DOI: 10.5517/ccdc.csd.cc2pkgg6; (*l*) CCDC 2489439: Experimental Crystal Structure Determination, 2025, DOI: 10.5517/ccdc.csd.cc2pkgh7; (*m*) CCDC 2489440: Experimental Crystal Structure Determination, 2025, DOI: 10.5517/ccdc.csd.cc2pkgj8; (*n*) CCDC 2489441: Experimental Crystal Structure Determination, 2025, DOI: 10.5517/ccdc.csd.cc2pkgk9; (*o*) CCDC 2489442: Experimental Crystal Structure Determination, 2025, DOI: 10.5517/ccdc.csd.cc2pkglb; (*p*) CCDC 2489443: Experimental Crystal Structure Determination, 2025, DOI: 10.5517/ccdc.csd.cc2pkgmc; (*q*) CCDC 2489444: Experimental Crystal Structure Determination, 2025, DOI: 10.5517/ccdc.csd.cc2pkgnd; (*r*) CCDC 2489445: Experimental Crystal Structure Determination, 2025, DOI: 10.5517/ccdc.csd.cc2pkgpf; (*s*) CCDC 2489446: Experimental Crystal Structure Determination, 2025, DOI: 10.5517/ccdc.csd.cc2pkgqg.